

Review

# Quasi-Optical Theory of Relativistic Cherenkov Oscillators and Amplifiers with Oversized Electrodynamical Structures

Andrey Malkin <sup>1,2</sup>, Naum Ginzburg <sup>1,2,\*</sup> , Vladislav Zaslavsky <sup>1,2</sup>, Ilya Zheleznov <sup>1</sup> and Alexander Sergeev <sup>1</sup>

<sup>1</sup> Department of Advanced School of General and Applied Physics, Institute of Applied Physics RAS, Nizhny Novgorod 603950, Russia; malkin@appl.sci-nnov.ru (A.M.); zas-vladislav@appl.sci-nnov.ru (V.Z.); vicont\_18@mail.ru (I.Z.); sergeev@appl.sci-nnov.ru (A.S.)

<sup>2</sup> Department of Radiophysics, Nizhny Novgorod State University, Nizhny Novgorod 603950, Russia

\* Correspondence: ginzburg@ipfran.ru

**Abstract:** Using the quasi-optical approach, we investigate wave propagation along the periodically corrugated surfaces and their interaction with rectilinear relativistic electron beams (REBs). At the periodical structure, the field can be expanded into a series of spatial harmonics, which, in the case of shallow corrugations, represent paraxial wavebeams with mutual coupling described within the method of effective surface magnetic currents. We present the dispersion equation for the normal waves. Two limit cases can be recognized: in the first one, the frequency is far from the Bragg resonance and the wave propagation can be described within the impedance approximation with the field presented as a sum of the fundamental slow wave and its spatial harmonics. In the interaction with a rectilinear REB, this corresponds to the convective instability of particles' synchronism with the fundamental (0th) or higher spatial harmonics (TWT regime), or the absolute instability in the case of synchronism with the  $-1$ st harmonic of the backward wave (BWO regime). In the latter case, at the frequencies close to the Bragg resonance, the field is presented as two antiparallel quasi-optical wavebeams, leading to the absolute instability used in the surface-wave oscillators operating in the  $\pi$ -mode regime. Based on the developed theory, we determine the main characteristics of relativistic Cherenkov amplifiers and oscillators with oversized electrodynamic systems. We demonstrate the prospects for the practical implementation of relativistic surface-wave devices in submillimeter wavebands.

**Keywords:** surface wave; sub-THz radiation sources; quasi-optical theory; 3D simulations



**Citation:** Malkin, A.; Ginzburg, N.; Zaslavsky, V.; Zheleznov, I.; Sergeev, A. Quasi-Optical Theory of Relativistic Cherenkov Oscillators and Amplifiers with Oversized Electrodynamical Structures. *Electronics* **2022**, *11*, 1197. <https://doi.org/10.3390/electronics11081197>

Academic Editor: Minh-Khai Nguyen

Received: 31 January 2022

Accepted: 2 April 2022

Published: 9 April 2022

**Publisher's Note:** MDPI stays neutral with regard to jurisdictional claims in published maps and institutional affiliations.



**Copyright:** © 2022 by the authors. Licensee MDPI, Basel, Switzerland. This article is an open access article distributed under the terms and conditions of the Creative Commons Attribution (CC BY) license (<https://creativecommons.org/licenses/by/4.0/>).

## 1. Introduction

Cherenkov-stimulated emissions from rectilinear relativistic electron beams (REBs) in periodically corrugated waveguides have been widely used in radiation sources providing GW power output in centimeter wavebands and up to MW in the sub-millimeter wavelength range [1–25]. The radiated electromagnetic fields propagating in a periodic structure, according to the Floquet theorem, can be expanded into a series of harmonics, one of which interacts with an electron beam under the Cherenkov-type synchronism conditions:

$$\omega - hv_{\parallel} = s\bar{h}v_{\parallel}, \quad (1)$$

where  $v_{\parallel}$  is the particle translational velocity,  $\omega$  is the radiation frequency,  $h$  is the longitudinal wavenumber of the fundamental harmonic,  $\bar{h} = 2\pi/d$ ,  $d$  is the structure's period, and  $s$  is the number of synchronous spatial harmonics. The main types of interaction regimes in Cherenkov oscillators and amplifiers are illustrated by the dispersion diagrams presented in Figure 1. For the realization of traveling wave tube (TWT) amplifiers [6,7], one can use either the interaction with the 1st ( $s = 1$ , point D1) or with the fundamental ( $s = 0$ , point A) [3,16,17] decelerated harmonic of the wave co-moving ( $hv_{\parallel} > 0$ ) with the beam. Among the oscillator schemes, first of all, the backward wave oscillator (BWOs) [1,2,4–15] should be

identified, where the electrons interact with the spatial harmonic of the wave propagating in a backward ( $h v_{\parallel} < 0$ , points C) direction. The orotron regime of interaction [5,26] should also be mentioned, in which the radiation frequency is close to the cutoff frequency of the operating mode ( $h \rightarrow 0$ , point E). Such regimes can also be referred to as operation regimes near the low-frequency edge of the transparency band or, in terms of a phase shift at one period of the structure, as  $2\pi$ -mode excitation regimes. The alternative is to operate in the vicinity of the high-frequency edge of the transparency band (point B) or  $\pi$ -mode excitation regimes. In the latter regime, the fundamental harmonic is excited and the formation of the surface wave takes place. Thus, such radiation sources are usually referred to as surface-wave oscillators (SWOs) [18–25]. In the theoretical and experimental investigations presented in [19,20], the term “multiwave Cherenkov oscillators” (MWCO) was also used.

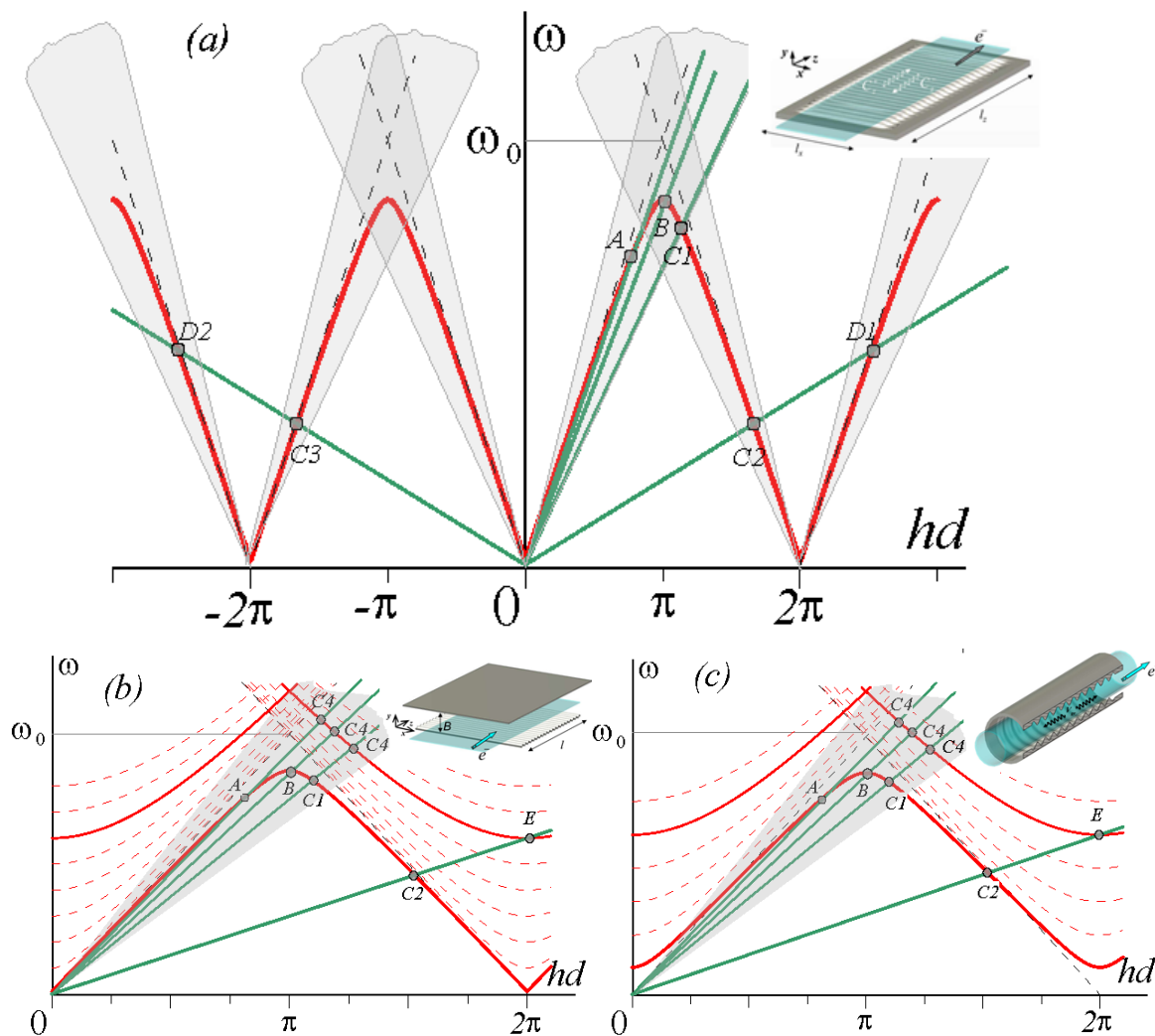


**Figure 1.** Dispersion diagrams of Cherenkov beam-wave interactions in periodically corrugated systems: (a) corrugated metal plate; (b) planar; and (c) cylindrical waveguides. Electron beam lines at different energies are shown in green, solid red curves mark the dispersion of the synchronous normal waves, dashed red curves correspond to the waveguide partial modes, and dashed black lines are the light lines. Point A's correspond to the TWT synchronisms with the fundamental harmonics, B are the  $\pi$  mode synchronisms, C are the BWO synchronisms, D mark the TWT synchronisms with the +1st harmonics, and E stand for the orotron regimes. Gray areas are the regions of quasi-optical approximation validity.

Between the distinguished regimes, there are no sharp boundaries: a variation in the particles' energy leads to a smooth shift of the synchronism point in the dispersion diagram from one regime to another (see Figure 1). However, in the development of the real experimental devices, one of the regimes is usually chosen as an operating one, whereas the others are considered to be the sources of parasitic excitation, usually related to operation at spurious modes with a transverse index differing from that of the chosen operation mode.

However, for the analysis presented in this paper, it is no less important that the previous theoretical models describing the indicated regimes are fairly different. The theory of such variants of relativistic devices, in which the transverse field structure can be assumed fixed and coinciding with one of the bulk modes of the metal or dielectric [27] waveguide, has been constructed somewhat thoroughly. This applies in the first place to TWT amplifiers [3] operating at the spatial harmonics and to the stationary [2] and non-stationary [28–31] theories of backward wave oscillators (BWOs), which, in addition to the form of particle motion equations, are similar to the theories of their weakly relativistic counterparts [32,33]. The applicability condition of these theoretical models under conditions of paraxial propagation of radiation, typical for TWT and BWO, is the limitation on the transverse dimensions of the waveguides by one or several wavelengths. For the significantly oversized structures, the fixed structure approximation can also be efficient in the analysis of the orotrons [34], which involves interaction at quasi-cutoff frequencies and the formation of the operating mode by Brillouin rays propagating in the transverse direction with respect to the electron's translational velocity. Similar to gyrotrons [35], selective excitation of a single quasi-cutoff mode with a fixed transverse structure is possible in orotrons. In these devices, synchronous interaction of the REB with a spatial harmonic of the operating mode takes place.

This paper is devoted to a theoretical description of relativistic Cherenkov-type radiation sources with oversized electro-dynamical systems. Implementation of oversized structures (i.e., those with transverse dimensions strongly exceeding the wavelength) is relevant for relatively long-wavelength bands (X-band) for the realization of ultra-high-power (multi-GW) pulsed radiation sources, and, even more so, for shorter-wavelength bands (W-band or G-band), where one needs to reduce the Ohmic losses and simultaneously provide a channel for the transportation of intense REBs.

Under such conditions, it is natural to use the quasi-optical approach for the description of radiation propagation [36–41]. The main simplified assumption, proposed in [36] and further developed in [37] and used in the presented analysis, is the approximation of relatively shallow corrugation depth in the scale of its period and wavelength. This assumption is justified by the experimental situation in the case of relativistic electron beam radiation when the Cherenkov-type synchronous interaction requires the wave to be decelerated only slightly. At the same time, the smallness of the corrugation allows the method of equivalent surface magnetic currents to be used, developed in [42]. At the corrugated structure, the field is expanded in a series of spatial harmonics; each one of them is represented by a paraxial wavebeam described, within the quasi-optical approach, by parabolic-type equations.

Thus, this review contains the main concepts of the theory of Cherenkov-type oscillators and amplifiers with oversized electro-dynamical systems, most of which involve the slowing-down of the fundamental spatial harmonics, which makes the conventional representation of the mode field as the bulk waveguide mode incorrect. First, TWT at the fundamental slowed-down harmonic and relativistic surface-wave oscillators (SWOs) are discussed. Despite numerous experimental realizations of such devices [18–25], consistent linear and non-linear theories had been lacking, despite some semi-phenomenological models describing the formation of the surface wave by the parabolic equations constructed based on the dispersion law [31,43]. At the same time, these regimes recently became more relevant for experiments [21–25] due to the advancement of the Cherenkov-type sources into the shorter-wavelength bands, as these regimes are characterized by the fairly high coupling of the electrons with the wave. Besides, the formation of the surface wave

ensures the regularity of the radiation pattern along the normal (with respect to the surface) coordinate, thus allowing the oversized waveguides to be used. In short-wavelength bands, the description of conventional regimes of interaction at the spatial harmonics has some specific features. At large oversize factors, slowing down of the fundamental harmonic can become significant. As a result, a surface wave is formed possessing the spatial harmonics that can be involved in synchronous interactions with the REB both in TWT (+1st harmonic) and BWO (−1st harmonic) regimes.

Throughout the paper, we consider two main geometries of Cherenkov radiation sources, the planar geometry and the cylindrical one. Planar geometry [43–47], albeit somewhat exotic for experimental realization, is much simpler for theoretical consideration and is used as the basic one. The more conventional cylindrical systems in the case of a fairly large oversize can be described in the quasi-planar approximation. The differences between planar and cylindrical models are specifically emphasized. It should be noted that most of the theoretical results presented here were verified by direct 3D PIC simulations [36–41], although we opt to leave the comparisons out of the current presentation.

Accordingly, the paper is organized as follows. Section 2 is dedicated to the electro-dynamical features of the corrugated structures in the absence of the electron beam. A dispersion equation was obtained for the normal surface waves. Specific features of surface wave formation in planar and cylindrical waveguides are presented; in the latter case, a criterion of surface-wave existence is obtained. The case of near-cutoff modes is considered separately. An analytical description of the formation of high-quality longitudinal modes in finite-length corrugated structures is given. In Section 3, the self-consistent system of equations of electron-wave synchronous interaction with the field of one of the harmonics is obtained in the most general form for the planar geometry. We show that these equations describe TWT, BWO,  $\pi$ -mode, and orotron operation regimes and in some cases can be reduced to conventional fixed-structure equations. Lateral mode selection is considered using a 3D model. We also discuss the excitation of the surface wave by extended electron bunches in super-radiant regimes. In Section 4, the above concepts are applied to cylindrical structures. In the conclusion, a brief overview of the novel theoretical and experimental concepts of surface-wave devices utilizing complex gratings proposed on the basis of the quasi-optical theory is given.

## 2. Electrodynamics of Weakly Corrugated Planar and Cylindrical Waveguides

### 2.1. Dispersion Characteristics of Normal Waves near a Single Periodically Corrugated Plate

We start with the analysis of the dispersion characteristics of the normal waves propagating along the corrugated metal plate (Figure 2) characterized by displacement,

$$b(z) = b_{\sim} \cos(\bar{h}z). \quad (2)$$

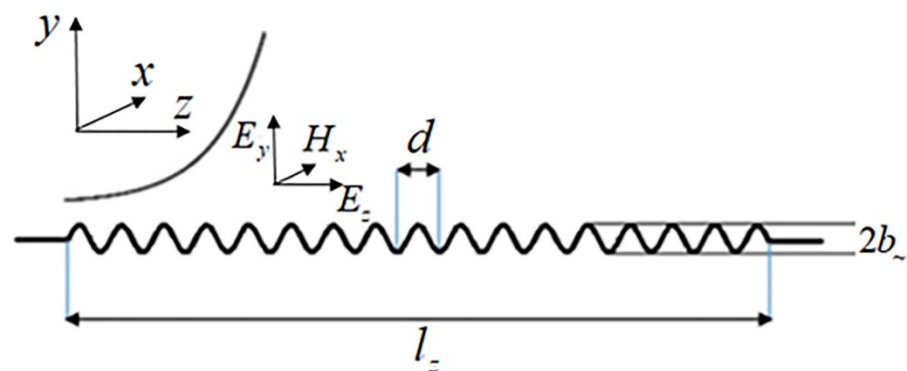


Figure 2. Schematic of a corrugated planar section.

We assume that the corrugation is shallow both in the scale of its period  $b \ll d$  and the radiation wavelength  $b \ll \lambda$ . Consider the TM polarized field with the following components

$$H_x = \text{Re}\left(H_x^\omega e^{i\omega t}\right), E_y = \text{Re}\left(E_y^\omega e^{i\omega t}\right), E_z = \text{Re}\left(E_z^\omega e^{i\omega t}\right). \tag{3}$$

As shown in [36–42], such a corrugated plate can be substituted by a regular surface  $y = 0$  with an effective surface magnetic current

$$j_x^m = \frac{c}{4\pi} \left( \frac{\partial}{\partial z} \left( b(z) E_y^\omega \right) - i \frac{\omega}{c} b(z) H_x^\omega \right). \tag{4}$$

In the planar geometry under consideration, the Maxwell equation for monochromatic fields with the inclusion of a magnetic current (4) can be reduced to a single equation for  $H_x$  component,

$$\Delta H_x^\omega + \frac{\omega^2}{c^2} H_x^\omega = i\omega \frac{4\pi}{c^2} j_x^m \delta(y), \tag{5}$$

where  $\delta(y)$  is the delta function. Due to the periodicity of the coefficients, the paraxial eigenwaves of Equation (5) are presented as a composition of spatial harmonics (Floquet expansion)

$$H_x^\omega = \sum_{s=-\infty}^{+\infty} H_s(z, y) e^{-i(k+s\bar{h})z}, \tag{6}$$

where  $k = \omega/c$  and  $H_s(z, y)$  are slowly varying in the scale of the period. Correspondingly, the components of the electric field  $E_y^\omega = -\frac{i}{k} \frac{\partial H_x^\omega}{\partial z}$  and  $E_z^\omega = \frac{i}{k} \frac{\partial H_x^\omega}{\partial y}$  can be written down as:

$$E_y^\omega = -\sum_{s=-\infty}^{+\infty} \frac{k+s\bar{h}}{k} H_s e^{-i(k+s\bar{h})z}, E_z^\omega = \frac{i}{k} \sum_{s=-\infty}^{+\infty} \frac{\partial H_s}{\partial y} e^{-i(k+s\bar{h})z}. \tag{7}$$

Note here that from a Floquet theorem’s point of view, the numeration of harmonics in (6–7) is somewhat arbitrary and can be shifted by any integer  $S$  using the substitution  $H_{s'} = H_s e^{iS\bar{h}z}$ ; by default, we assume the fundamental harmonic  $H_0$  to be slow in the scale of the Bragg wavenumber,  $|\partial H_0/\partial z| \ll |\bar{h}H_0|$ ; moreover, the sign of  $s$  can also be changed by changing the sign of  $\bar{h}$ . For shallow corrugations, the series (6–7) can be limited by the three lowest harmonics (0th, –1st, and 1st); substitution in (5), after neglecting the rapidly varying terms, yields

$$\frac{\partial H_0}{\partial z} + \frac{i}{2k} \frac{\partial^2 H_0}{\partial y^2} = -i\alpha \delta(y) (H_1 - H_{-1}), \tag{8}$$

$$\frac{\partial H_1}{\partial z} + \frac{i}{2(\bar{h}+k)} \frac{\partial^2 H_1}{\partial y^2} - i \frac{\bar{h}^2 + 2k\bar{h}}{2(\bar{h}+k)} H_1 = -i\alpha \frac{k}{\bar{h}+k} \delta(y) H_0, \tag{9}$$

$$-\frac{\partial H_{-1}}{\partial z} + \frac{i}{2(\bar{h}-k)} \frac{\partial^2 H_{-1}}{\partial y^2} - i \frac{\bar{h}^2 - 2k\bar{h}}{2(\bar{h}-k)} H_{-1} = i\alpha \frac{k}{\bar{h}-k} \delta(y) H_0, \tag{10}$$

where  $\alpha = b\bar{h}/4$  is the coupling coefficient. Presenting the solutions of the linear system (8–10) as  $H_{0,\pm 1} \sim \exp(i\Gamma z - g_{0,\pm 1}y)$ , we find the transverse decrements  $g_{0,\pm 1}$  and corresponding wavenumbers  $\kappa_{0,\pm 1} = ig_{0,\pm 1}$  of the harmonics:

$$\kappa_0 = ig_0 = i\sqrt{2k\Gamma}, \kappa_{\pm 1} = ig_{\pm 1} = i\sqrt{\left(k \pm \bar{h}\right)^2 - k^2 + 2\left(k \pm \bar{h}\right)\Gamma}. \tag{11}$$

These decrements are bound by the dispersion relation

$$g_0 = 4k^2\alpha^2\left(\frac{1}{g_1} + \frac{1}{g_{-1}}\right), \tag{12}$$

which can be treated as an equation allowing to find the  $\Gamma(k)$  dependence. The total longitudinal wavenumber of the fundamental harmonic, according to Equations (6) and (11), is

$$h(k) = k + \Gamma(k) = k + \frac{g_0^2}{2k}. \tag{13}$$

Figure 3 shows the dispersion characteristics  $h(k)$  of the normal waves at various values of the coupling coefficient. Obviously, these curves lie beneath the light lines (shown in dash-dot), so the corresponding waves are slow; the transverse decrement is purely real so these solutions correspond to evanescent (surface) waves. The amendment  $\Gamma$  of the wavenumber characterizes the deceleration of the surface wave:

$$v_{ph}/c = k/h \approx 1 - \Gamma/k. \tag{14}$$

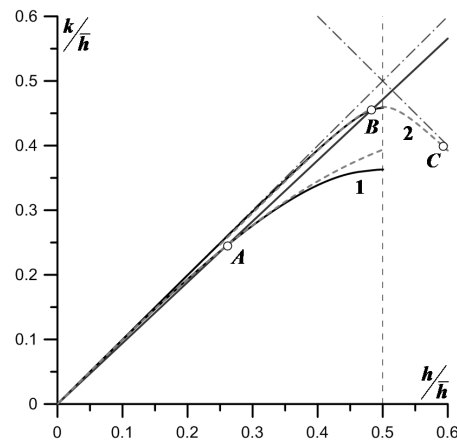


**Figure 3.** Dispersion curves of the surface waves determined by Equation (12): curve 1 at  $\alpha = 0.4$ , curve 2 at  $\alpha = 0.2$ . Dashed line near curve 1 corresponds to the impedance approximation Equations (17) and (18), dashed line near curve 2 corresponds to the approximation of counter-propagating wavebeams (26) (Equation (22)). Similarly to Figure 1 caption, point A corresponds to the TWT synchronism with the fundamental harmonics, B denotes the  $\pi$  mode synchronism, C is the BWO synchronism.

Further, it is important to distinguish the two limit cases:

(A) In the first case, the wave frequency is far from the Bragg resonance frequency  $\omega_0 = c\bar{h}/2$ ; here  $2(k \pm \bar{h})\Gamma \ll (k \pm \bar{h})^2 - k^2$ , and (9) yields  $g_{\pm 1} \approx \sqrt{(k \pm \bar{h})^2 - k^2}$ . Under such conditions the derivatives with respect to  $z$  can be neglected in Equations (8) and (9) which then are integrated as

$$H_{\pm 1} = \pm 2\alpha \frac{k}{g_{\pm 1}} H_0 e^{-g_{\pm 1}y}, \tag{15}$$

so Equation (10) is reduced to a single equation

$$\frac{\partial H_0}{\partial z} + \frac{i}{2k} \frac{\partial^2 H_0}{\partial y^2} + i\chi\delta(y)H_0 = 0. \tag{16}$$

Here, we introduce the surface impedance

$$\chi = 2\alpha^2 \left( \frac{k}{\sqrt{(k + \bar{h})^2 - k^2}} + \frac{k}{\sqrt{(k - \bar{h})^2 - k^2}} \right). \tag{17}$$

Further, we refer to this approximation as an impedance approximation [41], as Equation (16) yields an impedance-type relation between the electric and magnetic field amplitudes on the surface:

$$\frac{i}{2k} \frac{\partial H_0}{\partial y} \Big|_{y=0} = -i\chi H_0|_{y=0}, \text{ or } E_z^\omega = -2i\chi H_x^\omega.$$

In the impedance approximation, the dispersion Equation (12) is simplified to the form

$$\Gamma = 2k\chi^2. \tag{18}$$

The transverse decrement of the 0th harmonic is proportional to the impedance,  $g_0 = 2k\chi$ . In Figure 3, at  $\alpha = 0.4$ , a solid curve shows the dispersion of the normal surface wave determined by Equation (14) while the dashed line is the one obtained using Equation (20); far from the Bragg resonance the curves are very close, whereas at  $k \approx \bar{h}/2$ , they diverge as  $\chi(k) \rightarrow \infty$ .

(B) In the second limit case, near the intersection of the partial-wave curves of the 0th and  $-1$ st spatial harmonics, the wave frequency is close to the Bragg frequency,

$$|\bar{h} - 2k| \ll \bar{h}. \tag{19}$$

Here  $g_{-1} \ll g_1$ , and the dispersion Equation (10) transforms to

$$\Gamma = 8k^3\alpha^4 \frac{1}{g_{-1}^2}, \tag{20}$$

which is equivalent to dropping Equation (9) for the  $+1$ st harmonic from (8–10). Introducing the shifts from the Bragg frequency and wavenumber,

$$\frac{\Omega}{c} = \frac{\bar{h}}{2} - k, \tilde{\Gamma} = \Gamma - \frac{\Omega}{c}, \tag{21}$$

we put the dispersion Equation (20) to its equivalent symmetric form (wave over  $\Gamma$  is further omitted)

$$\left( \frac{\Omega}{c} \right)^2 - \tilde{\Gamma}^2 = \bar{h}^2 \alpha^4. \tag{22}$$

The solution of Equation (22) is also shown in Figure 3 as a dashed curve. Accordingly, using (21) and neglecting the  $+1$ st harmonic, one might introduce the symmetric notations for the fields of coupled harmonics

$$C_+ = H_0 e^{-i\frac{\Omega}{c}z}, C_- = H_{-1} e^{-i\frac{\Omega}{c}z} \tag{23}$$

and put the Equations (8)–(10) to the form:

$$\pm \frac{\partial C_\pm}{\partial z} + i\frac{\Omega}{c}C_\pm + \frac{i}{\bar{h}} \frac{\partial^2 C_\pm}{\partial y^2} = i\alpha\delta(y)C_\mp. \tag{24}$$

The system (24) can be readily generalized on non-stationary processes by replacing  $\Omega \rightarrow -i\partial/\partial t$ ; transformations (21) and (23) then mean that the carrier frequency in (3) is chosen to be equal to the Bragg frequency  $\omega = \omega_0 = \bar{h}c/2$  while the field amplitudes are

considered to be slowly varying in time. Another obvious generalization can be undertaken by the inclusion of the second transverse coordinate ( $x$ ) in consideration. According to the initial Helmholtz Equation (5), the second derivative with respect to  $x$  would appear with the same sign and the same coefficient as  $\partial^2/\partial y^2$ . One more generalization is the inclusion of the Ohmic losses according to the Leontovich boundary condition [48]. Thus, the more general equations describing the spatio-temporal dynamics of the field under the conditions (19) of the Bragg resonance would be as follows:

$$\pm \frac{\partial C_{\pm}}{\partial z} + \frac{1}{c} \frac{\partial C_{\pm}}{\partial t} C_{\pm} + \frac{i}{\bar{h}} \frac{\partial^2 C_{\pm}}{\partial y^2} + \frac{i}{\bar{h}} \frac{\partial^2 C_{\pm}}{\partial x^2} + i\sigma C_{\pm} \delta(y) = i\alpha \delta(y) C_{\mp}. \tag{25}$$

Here  $\sigma = \sqrt{i/2k} d_{skin}$ ,  $d_{skin}$  is the skin depth; parabolic-type operators on the left-hand side of Equation (25) describe the diffraction of the wavebeams with respect to the transverse coordinates. It is important that under conditions (19), the symmetric Equation (25) describe the mutual scattering of the 0th and the  $-1$ st harmonics represented as two counter-propagating quasi-optical wavebeams (compare to Equation (6)):

$$H_x = \text{Re} \left( C_+(x, y, z, t) e^{-i\frac{\bar{h}}{2}z} + C_-(x, y, z, t) e^{i\frac{\bar{h}}{2}z} \right) e^{i\frac{\bar{h}c}{2}t} \tag{26}$$

### 2.2. Dispersion Characteristics of Normal Waves in a Planar Corrugated Waveguide

In a planar waveguide with a width of  $b$  (Figure 1b), with a corrugation (2) on one of the walls, and the second in the perfect metal described by the boundary condition  $E_z^\omega = \frac{i}{k} \frac{\partial H_x^\omega}{\partial y} = 0$ , Equations (8)–(10) would still be valid. According to the boundary conditions, their solution should be presented as

$$H_{0,\pm 1} = \tilde{H}_{0,\pm 1} ch[g_{0,\pm 1}(y - b)] e^{-i\Gamma z}. \tag{27}$$

Similarly to Equations (11)–(13), we obtain the dispersion equation for the normal waves:

$$\Gamma \tanh^2 \sqrt{2\Gamma} kb = 8k^3 \alpha^4 \left( \frac{1}{g_+ \tanh g_+ b} + \frac{1}{g_- \tanh g_- b} \right)^2. \tag{28}$$

At  $\alpha = 0$ , (28) and (13) yield a dispersion relation for the waves in a planar corrugated waveguide,  $h_n(k) = k + \frac{1}{2k} \left( \frac{n\pi}{b} \right)^2$ , where  $n$  is an integer (Figure 1b). This dispersion corresponds to a set of regular waveguide modes with cutoff frequencies of  $\frac{n\pi c}{b}$ , which we usually refer to as partial modes. Note, however, that the real dispersion law in the waveguide is hyperbolic,  $h_n(k) = \sqrt{h^2 + \left( \frac{n\pi}{b} \right)^2}$ . According to the theory constructed above, Equation (28) and the dispersion laws that follow from it are valid in quasi-optical approximation, at  $\frac{n\pi}{b} \ll h$ , i.e., at the frequencies far from the cutoff.

It is also important to note that in the planar geometry, the lowest TEM mode ( $n = 0$ ) has zero cutoff and the vacuum dispersion law,  $h_{n=0}(k) = k$ . Thus, at  $\alpha \neq 0$ , this mode corresponds to the surface wave in a semi-infinite system described above. Under the conditions (17) of the Bragg resonance, using the transformations (21) and (23), Equation (28) can be formulated in terms of transverse decrements  $g_+ = g_0 = \sqrt{-\bar{h}(\Omega/c + \Gamma)}$ ,  $g_- = g_{-1} = \sqrt{-\bar{h}(\Omega/c - \Gamma)}$  as

$$g_+ g_- \tanh(g_+ b) \tanh(g_- b) = -\bar{h}^2 \alpha^2 \tag{29}$$

In the wide waveguide,  $e^{|g_{\pm} b|} \gg 1$  (Figure 4a near  $\Gamma = 0$ ), one can put  $\tanh(g_{\pm} b) \approx 1$  and neglect the second wall, thus transforming the dispersion Equation (29) into (22). The

opposite limit is a waveguide narrow in the scale of field decrement,  $|g_{\pm}b| \ll 1$ , (Figure 4b near  $\Gamma = 0$ ), when  $\tanh(g_{\pm}b) \approx g_{\pm}b$ , and Equation (28) yields

$$\frac{\Omega^2}{c^2} - \Gamma^2 = \frac{a^2}{4b^2}.$$

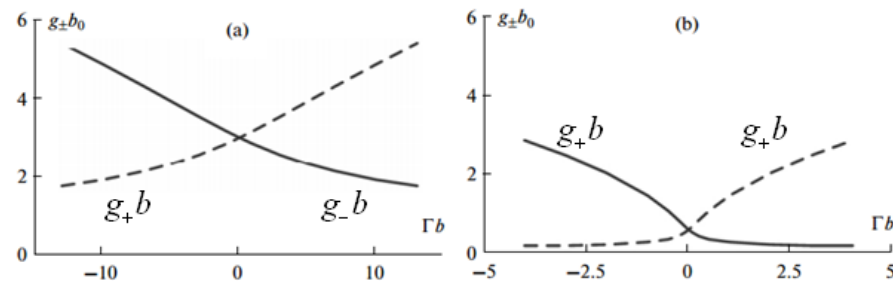


**Figure 4.** Absolute values of transverse wavenumbers of the lowest planar waveguide mode found from Equation (29) vs. shift of the longitudinal wavenumber from the Bragg resonance for different widths of the waveguide: (a)  $\alpha\bar{h}b = 6$ , (b)  $\alpha\bar{h}b = 0.6$ .

This is a well-known equation describing the coupling of two counter-propagating TEM modes with fixed transverse field structures in a planar waveguide under conditions (19).

Another important limit of Equation (28) is the case of non-resonant wave coupling realized at large  $|\Gamma b|$ . Here, one of the transverse decrements tends to zero (Figure 4b at  $|\Gamma b| \gg 1$ ). Let us put for definiteness  $|g_+b| \gg 1$ , but  $|g_-b| \ll 1$ , which is true at  $\Gamma > 0$ , and transform Equation (29) to

$$\sqrt{(-\Omega + \Gamma)(-\Omega - \Gamma)} = \frac{\sqrt{\bar{h}}\alpha^2}{b}.$$

Substituting expressions (27) into Equations (8)–(10), one can put down the field of the normal wave as a combination of the TEM mode and its evanescent spatial harmonics propagating in the backward direction:

$$H_x = \text{Re}C_+ \left[ e^{i((\bar{h}c/2+\Omega)t+(\bar{h}/2+\Gamma)z)} + \frac{2\alpha\bar{h} \cosh(g_+y)}{g_+ \sinh(g_+b)} e^{i((\bar{h}c/2+\Omega)t-(\bar{h}/2-\Gamma)z)} \right].$$

Dispersion Equation (29) describes not only the dispersion of the lowest surface mode, which exists in the system at a large gap  $b$ , but also several of the next transverse modes propagating in a finite-gap waveguide, far from their cutoff frequencies. Corresponding characteristics are presented in Figure 5.

Note that for the solution located beneath the light lines, the transverse wavenumbers  $\kappa_{\pm} = ig_{\pm}$  are purely imaginary so this solution corresponds to the evanescent mode. For solutions above the light lines, according to (29) the transverse wavenumber is purely real so these solutions correspond to the bulk modes of the planar waveguide with different transverse indexes. If the second wall is removed,  $b \rightarrow \infty$ , these solutions transform to continuous-spectrum solutions.

Far from Bragg resonances, the  $n$ th solution of Equation (29) corresponds to a combination of the  $n$ th mode of the planar waveguide ( $n$  variations over  $y$ ) for the component  $C_+$  and a fast-decreasing spatial harmonic for the component  $C_-$  (to the left of the resonances). To the right,  $C_+$  and  $C_-$  are swapped. Dispersion characteristics are split in the Bragg resonance areas due to the interaction of partial waves with various transverse indexes.

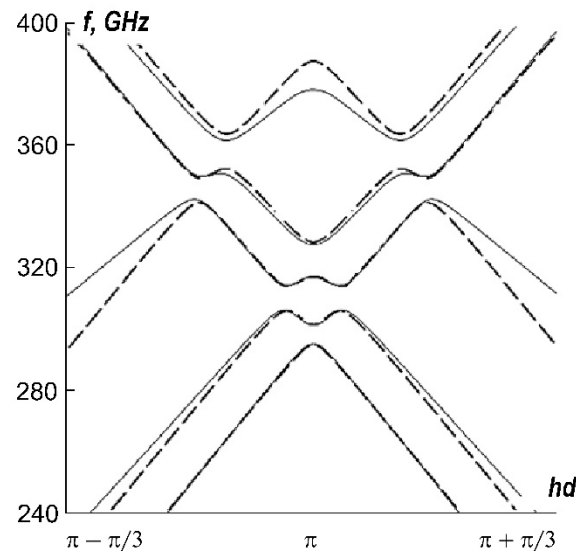


**Figure 5.** Dispersion diagram describing wave propagation in a planar waveguide with a single corrugated wall with a period of  $d = 0.5$  mm and an amplitude of  $0.025$  mm. The gap between planes  $b = 1.25$  mm. Dashed curves were obtained from Equation (29) and solid curves were obtained by means of numerical simulation with the use of CST Microwave Studio.

For comparison, solid curves in Figure 5 show the dispersion characteristics obtained in direct simulations using CST MICROWAVE STUDIO software; near the Bragg resonance of the zeroth modes, i.e., at  $\Omega/\omega \leq 0.1$ ,  $\Gamma/k \leq 0.1$ , qualitative and quantitative correspondence is fine.

*Near-cutoff modes in corrugated waveguides.* As noted above, the consideration based on presenting the field harmonics as quasi-optical wavebeams propagating along the corrugated surface is inapplicable near the cutoff frequencies (point E in Figure 1b) of higher ( $n > 1$ ) waveguide modes. Nevertheless, the above formalism can be modified in order to include the near-cutoff waves. Indeed, consider the case when the 0th harmonic in the Floquet expansion has  $h = 0$ , and write, correspondingly (compare to Equation (6)),

$$H_x^\omega = H_0(z, y, t) + H_1(y, z, t)e^{-i\bar{h}z} + H_{-1}(y, z, t)e^{i\bar{h}z} \tag{30}$$

Accordingly, taking into account (4), (7), and (30), the surface magnetic current can be put down as (all the fields in the right-hand part are taken at  $y = 0$ )

$$j_x^m = -i\frac{cb_\sim}{8\pi} \left( e^{i\bar{h}z}\bar{h}H_0 + e^{-i\bar{h}z}\bar{h}H_0 + \bar{h}(H_1 + H_{-1}) \right)$$

Substituting this expression into (5) and equating the coefficients with the corresponding exponents, we come up with a system of coupled-mode equations (compare to (8); note that here we cannot neglect the second derivative of  $H_0$ ):

$$\begin{aligned} \bar{h}^2 H_0 - 2i\bar{h}\frac{1}{c}\frac{\partial H_0}{\partial t} + \frac{\partial^2 H_0}{\partial z^2} + \frac{\partial^2 H_0}{\partial y^2} &= \frac{\bar{h}^2 b_\sim}{2}\delta(y)(H_1 + H_{-1}) \\ \frac{\partial H_1}{\partial z} + \frac{1}{c}\frac{\partial H_1}{\partial t} + \frac{i}{2\bar{h}}\frac{\partial^2 H_1}{\partial y^2} &= -i\frac{\bar{h}b_\sim}{4}H_0\delta(y) \\ -\frac{\partial H_{-1}}{\partial z} + \frac{1}{c}\frac{\partial H_{-1}}{\partial t} + \frac{i}{2\bar{h}}\frac{\partial^2 H_{-1}}{\partial y^2} &= -i\frac{\bar{h}b_\sim}{4}\delta(y)H_0 \end{aligned} \tag{31}$$

Note that the spectrum of the quasi-cutoff modes is significantly rarefied compared to the propagating waves; we can assume that only one quasi-cutoff mode  $H_0 = F_n(z) \cos \frac{n\pi y}{b}$  is excited, and reduce Equation (31) to the form:

$$\begin{aligned} \frac{1}{c} \frac{\partial}{\partial t} F_n - \frac{i}{2\bar{h}} \frac{\partial^2 F_n}{\partial z^2} + \frac{i}{2\bar{h}} \left( \bar{h}^2 - \left( \frac{n\pi}{b} \right)^2 \right) F_n &= -i \frac{\bar{h}b}{b} (H_1(0, z) + H_{-1}(0, z)), \\ \frac{\partial H_1(y, z)}{\partial z} + \frac{1}{c} \frac{\partial H_1(y, z)}{\partial t} + \frac{i}{2\bar{h}} \frac{\partial^2 H_1(y, z)}{\partial y^2} &= -i \frac{\bar{h}b}{4} \delta(y) F_n, \\ -\frac{\partial H_{-1}(y, z)}{\partial z} + \frac{1}{c} \frac{\partial H_{-1}(y, z)}{\partial t} + \frac{i}{2\bar{h}} \frac{\partial^2 H_{-1}(y, z)}{\partial y^2} &= -i \frac{\bar{h}b}{4} \delta(y) F_n, \end{aligned} \tag{32}$$

Although the cutoff mode has infinite phase velocity, its harmonics are subliminal and can be synchronous to electron beams. This synchronism is being utilized in orotrons [5,26,34,43]. Equation (32) is governed by geometrical detuning

$$\delta_g = \frac{\bar{h}^2 - \left( \frac{n\pi}{b} \right)^2}{2\bar{h}} = \frac{\pi(4b^2 - n^2d^2)}{2db^2} \tag{33}$$

When  $|\delta_g| \ll \bar{h}$ , Equation (32) describes the mutual coupling of quasi-cutoff and propagating waves used in a so-called advanced Bragg resonator for the provision of transverse mode selection in free electron masers [49]. At  $|\delta_g| \sim \bar{h}$ , as shown below in Section 3.6, Equation (32) can be reduced to those describing the wave propagation in the orotron [34].

### 2.3. Dispersion Characteristics of Normal Waves in Oversized Cylindrical Waveguides with Azimuthally Symmetric Corrugation

For high-current REBs, the tubular geometry of the electrodynamic systems is preferable compared to the planar systems considered above, as it allows for the formation of the beams with a more uniform distribution of density with respect to the transverse (azimuthal) coordinate. Accordingly, most of the experimental realizations of SWOs that had cylindrical symmetry were energized by tubular REBs. In particular, this applies to multiwave Cherenkov oscillators (MWCO), which provided the record output pulsed power values in the centimeter waveband [19,20].

*Dispersion characteristics of the symmetric modes at moderate oversize. The criterion of the surface-wave formation.*

At moderate oversize (diameter-to-wavelength ratio) factors, the azimuthally symmetric surface wave was excited in these oscillators exploiting the shallow azimuthally symmetric corrugation on the inner surface of a cylindrical waveguide,

$$r(z) = R + r_{\sim} \cos(\bar{h}z), \tag{34}$$

where  $r_{\sim}$  is its amplitude. In this Section, we investigate wave propagation in such systems, with axially symmetric TM-polarized waves having the following field components (cf. Equation (3)):

$$H_{\varphi} = \text{Re} \left( H_{\varphi}^{\omega} e^{i\omega_0 t} \right), \quad E_z = \text{Re} \left( E_z^{\omega} e^{i\omega_0 t} \right), \quad E_r = \text{Re} \left( E_r^{\omega} e^{i\omega_0 t} \right). \tag{35}$$

These fields can be expanded in a series of radial  $\text{TM}_{0n}$  modes of a regular cylindrical waveguide with a radius of  $R$ , which we refer to as partial modes, with a dispersion determined by  $\omega_{0n}(h) = c\sqrt{h^2 + \nu_{0n}^2}/R^2$  depicted in Figure 1c ( $\nu_{0n}$  are the roots of the zeroth order Bessel function  $J_0(\nu_{0n}) = 0$ ).

The corrugation provides coupling and mutual scattering of waves with wavenumbers  $h_+$  and  $h_-$  satisfying the Bragg condition  $h_+ - h_- = \bar{h}$ ; thus, a set of Bragg resonances emerges where the dispersion curves split (Figure 1c). At the lowest Bragg resonance, such splitting can lead to deceleration of the phase velocity and the formation of the evanescent wave, which can be excited by the electron beam.

This corrugation can also be substituted by the virtual surface magnetic current  $i_\phi^{\mu\omega_0}$  defined at the surface of a regular waveguide. In order to describe the excitation of the waves (33) by the effective surface magnetic current, the Maxwell equations can be reduced to a single equation for the magnetic field component  $H_\phi^\omega$

$$\frac{\partial}{\partial r} \left( \frac{1}{r} \frac{\partial (rH_\phi^\omega)}{\partial r} \right) + \frac{\partial^2 H_\phi^\omega}{\partial z^2} - 2ik_0 \frac{\partial H_\phi^\omega}{c\partial t} + k_0^2 H_\phi^\omega = -i \frac{4\pi k_0}{c} i_\phi^{\mu\omega} \delta(r - R), \tag{36}$$

and the relations binding the amplitudes of the electric and magnetic fields:

$$E_z^\omega = -\frac{i}{k_0} \frac{1}{r} \frac{\partial (rH_\phi^\omega)}{\partial r}, \quad E_r^\omega = \frac{i}{k_0} \frac{\partial H_\phi^\omega}{\partial z}.$$

Similarly to Equation (5), the solution of Equation (36) at the frequencies close to the Bragg resonance (see Figure 6a) can be presented as two counter-propagating TM-polarized quasi-optical wavebeams (26),

$$H_\phi^\omega = C_+(z, r, t)e^{-i\bar{h}z/2} + C_-(z, r, t)e^{i\bar{h}z/2}, \tag{37}$$

where  $C_+$  and  $C_-$  are the slow varying in space and time wave amplitudes. Further, we choose the carrier frequency equal to the frequency of the lowest partial  $TM_{01}$  mode corresponding to the Bragg wavenumber  $\omega_0 = \omega_{01}(\bar{h}/2) = c\sqrt{\bar{h}^2/4 + \nu_{01}^2/R^2}$ . Substituting (37) into (36) we obtain, after averaging, the coupled-wave equations describing the field propagation at frequencies close to the Bragg resonance (red dashed contour in Figure 6a):

$$\frac{\partial C_+}{\partial z} + \frac{2k_0}{\bar{h}} \frac{\partial C_+}{c\partial t} + \frac{i}{\bar{h}} \frac{\partial}{\partial r} \left( \frac{1}{r} \frac{\partial (rC_+)}{\partial r} \right) + i \frac{\nu_{01}^2}{\bar{h}R^2} C_+ = i\alpha\delta(r - R)C_- \tag{38}$$

$$-\frac{\partial C_-}{\partial z} + \frac{2k_0}{\bar{h}} \frac{\partial C_-}{c\partial t} + \frac{i}{\bar{h}} \frac{\partial}{\partial r} \left( \frac{1}{r} \frac{\partial (rC_-)}{\partial r} \right) + i \frac{\nu_{01}^2}{\bar{h}R^2} C_- = i\alpha\delta(r - R)C_+, \tag{39}$$

where

$$\alpha = \frac{r_1}{2} \left( \frac{\bar{h}}{2} + \frac{\nu_{01}^2}{\bar{h}R^2} \right) \tag{40}$$

is the coupling coefficient. Equations (38) and (39) have the solution  $C_\pm \sim J_1(\kappa_\pm r)e^{i\Omega t - i\Gamma z}$ ,  $|\Omega| \ll \omega$ ,  $|\Gamma| \ll h$  are amendments to the carrier frequency and axial wavenumber,

$$\kappa_\pm^2 = -g_\pm^2 = \frac{\nu_{01}^2}{R^2} \mp \bar{h}\Gamma + \frac{2\omega_0\Omega}{c^2} \tag{41}$$

are the complex transverse wavenumbers (note that  $\kappa_\pm = ig_\pm$  as defined previously) of the forward and the backward wavebeams bound by the dispersion equation describing the propagation of symmetric TM-polarized waves in a shallow corrugated cylindrical waveguide in the vicinity of the Bragg frequency:

$$\kappa_+ \kappa_- = \bar{h}^2 \alpha^2 \frac{J_1(\kappa_- r_0) J_1(\kappa_+ r_0)}{J_0(\kappa_- r_0) J_0(\kappa_+ r_0)}. \tag{42}$$

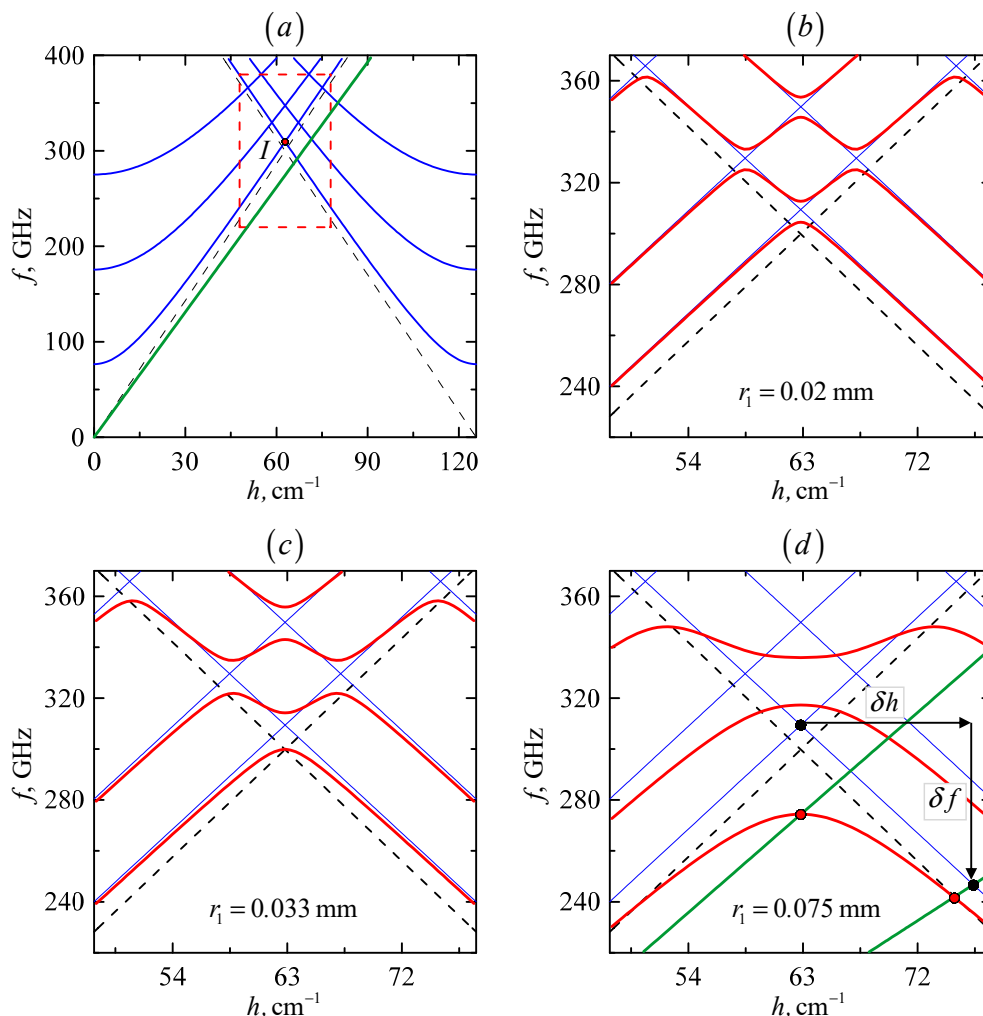


**Figure 6.** (a) Dispersion diagram  $f = \omega(h)/(2\pi)$  of the azimuthally symmetric TM partial modes in a corrugated waveguide (blue curves), black dashed lines denote the light lines  $f = hc/(2\pi)$ ; area of validity of the quasi-optical approximation is marked by a red dashed contour. (b–d) Dispersion curves of normal waves (red) split near the Bragg resonance at different corrugation amplitudes. Electron beam lines for different energies are shown in green;  $r_0 = 1.5$  mm,  $d = 0.5$  mm.

Solving (41) and (42), one finds a countable set of dispersion branches  $f_n = (\omega_0 + \Omega_n(\bar{h}/2 + \Gamma))/2\pi$  depicted in Figure 6 for different values of the coupling coefficient  $\alpha$ . Each solution corresponds to the  $n$ th axially symmetric mode  $TM_{0n}$  of the corrugated waveguide, which we refer to as normal waves. Most of these solutions correspond to fast waves with dispersion curves lying above the light cone, i.e., with phase velocities greater than the speed of light (see Figure 6b). However, at some parameters, the lowest normal  $TM_{01}$  wave might go below the light line, when both transverse wavenumbers  $\kappa_+$  and  $\kappa_-$  become imaginary and the wave is evanescent. Thus, Equations (41) and (42) yield a criterion on the geometry of the system allowing for the existence of the slow evanescent wave. At some value  $\alpha = \alpha^*$ , the topmost point of the dispersion curve of the lowest  $TM_{01}$  normal wave intersects with the light line at  $\Gamma = 0$  (see Figure 6c) and the phase velocity at this point is equal to the speed of light. Based on this, we derive the following criterion of the existence of the evanescent wave [40]:

$$r_1 \geq \frac{2d^2}{\pi^2 R}. \tag{43}$$

According to this relation, the larger the waveguide radius  $r_0$  is, the smaller the corrugation that is required for the formation of the evanescent wave. Note that in the planar waveguides considered previously in Section 2.2, there is no criterion similar to (43) and the slow wave emerges at an indefinitely small corrugation amplitude. Thus at  $\alpha > \alpha^*$  (Figure 6d), the  $TM_{01}$  normal wave becomes slow and can be excited in a Cherenkov-type interaction by a rectilinear electron beam.

It should be noted that in oversized waveguides,  $k_0R \gg 1$ ,  $\frac{v_{01}^2}{R^2}$  terms can be neglected in (36–39), and using the Bessel function asymptotic [50] at a large argument,  $J_m(\xi) \approx \sqrt{\frac{2}{\pi\xi}} \cos(\xi - \frac{2m+1}{4}\pi)$ , Equation (42) yields

$$\kappa_+\kappa_- = \bar{h}^2\alpha^2 \tan(\kappa_-R + \pi/4) \tan(\kappa_+R + \pi/4).$$

For evanescent waves ( $Re\kappa_{\pm} \neq 0$ ), the tangents in the right-hand part tend to unite at large values, so the dispersion is reduced to Equation (22) with a wave coupling coefficient of  $\alpha = \bar{h}r_{\sim}/4$ .

*Dispersion characteristics of normal waves in oversized waveguides with small curvature. Quasi-planar model.*

In the small-curvature oversized waveguides, when the mean waveguide radius  $R$  much exceeds the wavelength  $\lambda$ , beside the azimuthally symmetric modes, the non-symmetric modes would be excited by the electron beam. These can be described within the quasi-planar approximation by introducing the coordinate  $x = R\phi$  along the waveguide azimuth. In such an approximation, under conditions (19), the field at the corrugated surface can be presented as a sum of two TM-polarized wavebeams (26) with slow amplitudes  $C_{\pm}(x,y,z,t)$ , where the  $y$ -coordinate is reckoned in the normal direction from the corrugated metal surface. In the initial physical variables,  $H_x$  corresponds to the azimuthal component of the magnetic field while  $E_y$  and  $E_z$  determine the radial and axial electric field components, correspondingly.

The coupling of counter-propagating wavebeams (26) is described by the system of parabolic Equations (25) with the reference frequency chosen equal to the Bragg one,  $\omega_0 = \bar{h}c/2$ . Taking the cylindrical geometry into account, one should assume that the fields decay at  $y \rightarrow \infty$ . Besides, the cyclicity condition of solutions for Equations (25) with respect to the azimuthal coordinate is also required,

$$C_{\pm}(x + l_x, z, y, t) = C_{\pm}(x, z, y, t), \tag{44}$$

where  $l_x = 2\pi R$  is the system’s perimeter. This allows the fields to be expanded in the Fourier series,

$$C_{\pm}(x, z, y, t) = \sum_{m=-\infty}^{\infty} C_{\pm}^m(z, y, t)e^{2\pi imx/l_x}, \tag{45}$$

where each harmonic can be treated as a mode with an azimuthal index of  $m$ ,  $p = 2\pi/l_x$ . Equation (25) yields the system binding for the amplitudes of these modes:

$$\begin{aligned} \frac{\partial C_+^m}{\partial z} + \frac{\partial C_+^m}{c\partial t} + i\frac{\partial^2 C_+^m}{\bar{h}\partial y^2} - \frac{ip^2m^2}{\bar{h}}C_+^m &= i\alpha C_-^m\delta(y), \\ -\frac{\partial C_-^m}{\partial z} + \frac{\partial C_-^m}{c\partial t} + i\frac{\partial^2 C_-^m}{\bar{h}\partial y^2} - \frac{ip^2m^2}{\bar{h}}C_-^m &= i\alpha C_+^m\delta(y), \end{aligned} \tag{46}$$

For each azimuthal index  $m$ , these equations correspond to Equation (25) with a reference frequency shifted by  $p^2m^2$  and  $\partial/\partial x = 0$ .

Assuming that the waveguide radius is large in the scale of the decrement of the surface wave, we present the solutions of (46) at  $y > 0$  as  $C_{\pm}^m \sim \exp(i\Omega t - i\Gamma z - g_{\pm}^m y)$ , where

$$g_{\pm}^m = \sqrt{-\bar{h}\left(\frac{\Omega}{c} \mp \Gamma\right) + p^2m^2}$$

are the transverse decrements. Using the boundary conditions  $\left(\frac{\partial C_{\pm}^m}{\partial y} - \alpha \bar{h} C_{\mp}^m\right)\Big|_{y=0} = 0$  following from (46), we obtain the dispersion equation for the normal waves

$$g_+^m g_-^m = \bar{h}^2 \alpha^2 \text{ or } \frac{(\Omega - p^2 m^2 c / \bar{h})^2}{c^2} - \Gamma^2 = \bar{h}^2 \alpha^4. \tag{47}$$

For the azimuthally symmetric normal wave  $m = 0$ , Equation (47) coincides with Equation (22). As shown in Figure 7, the dispersion curves of the normal wave of the modes with various azimuthal indexes are similar to each other and lie beneath the light lines ( $\Omega < 0, |\Omega| < |\Gamma|$ ), i.e., these waves are slow. Correspondingly, the transverse wavenumbers  $\kappa_{\pm}^m = i g_{\pm}^m$  are purely imaginary, i.e., the fields are confined at the periodic structure with amplitudes decaying exponentially. At  $\Gamma = p^2 m^2 / \bar{h}$  all of the transverse decrements are equal to  $g_{\pm}^m = \bar{h}^2 r_{\sim} / 4$ .

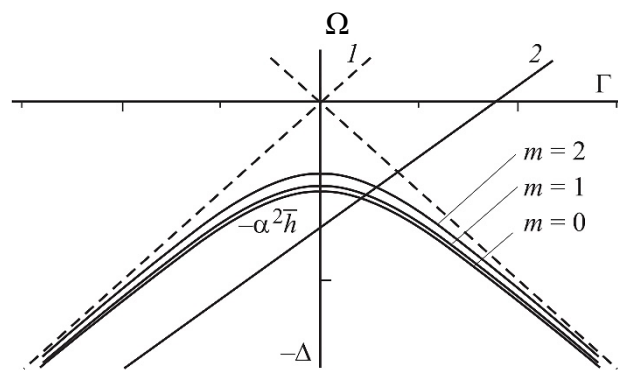


**Figure 7.** Dispersion curves of normal surface modes with different azimuthal indexes  $m$  in cylindrical oversized waveguides; the beam line is also shown.

2.4. Evanescent Eigenmodes in Finite-Length Periodic Structures

*Planar structures.* A section of a corrugated structure forms an open resonator with a length of  $l_z$  (Figure 2), which has a spectrum of modes with different longitudinal indexes. In order to find these modes, we supply Equations (25) with boundary conditions at the edges of the structure corresponding to the absence of external energy fluxes and of reflections for partial waves from the ends of the corrugation as well:

$$C_+(z = 0) = 0; C_-(z = l_z) = 0 \tag{48}$$

At  $\partial/\partial x = 0$ , solutions of Equations (25) and (48) depend only on two combinations of parameters, namely, on the normalized length  $L = \alpha^2 \bar{h} l_z$  and the normalized losses  $\sigma/\alpha$ . Assuming that the fields tend to zero at  $Y \rightarrow \infty$ , we seek the eigenmodes of (25) at a complex eigenfrequency of  $\Omega$  (which is a mismatch of the oscillation frequency from the Bragg frequency),  $C_{\pm} = \hat{C}_{\pm} e^{i\Omega t}$ .

In planar geometry, one can find the field structures and eigenfrequencies analytically. A Fourier transform of the fields over the  $Y$ -coordinate and the symmetry (or anti-symmetry) of solutions of Equations (25) and (48),  $\hat{C}_+(y, z) = \pm \hat{C}_-(y, l_z - z)$ , allows us to obtain a single integral equation [51] determining the eigenmodes:

$$\hat{C}_+(0, Z) = \sqrt{\frac{\bar{h}}{\pi i}} \int_0^z \frac{\pm \alpha \hat{C}_+(y = 0, l_z - z') + i \sigma \hat{C}_+(y = 0, z')}{\sqrt{z - z'}} e^{i \frac{\Omega(z'-z)}{c}} dz'. \tag{49}$$

This equation possesses an infinite discrete eigenmode spectrum, i.e., a set of complex values of  $\Omega$ . The frequencies and spatial profiles of eigenmodes were found numerically (Figure 8). The mode frequencies are located below the light line, so the real parts of the

mode eigenfrequencies are negative. They are marked with dots close to the dispersion curve in the lower part of Figure 8a for  $\alpha^2 \bar{h} l_z = 8.8$ , whereas the imaginary parts of these eigenfrequencies are shown as vertical lines in the upper part of the same figure. The quality factor  $Q = \omega_0(2\text{Im}\Omega)^{-1}$  of the fundamental mode is about 3 times higher than that of the second mode.

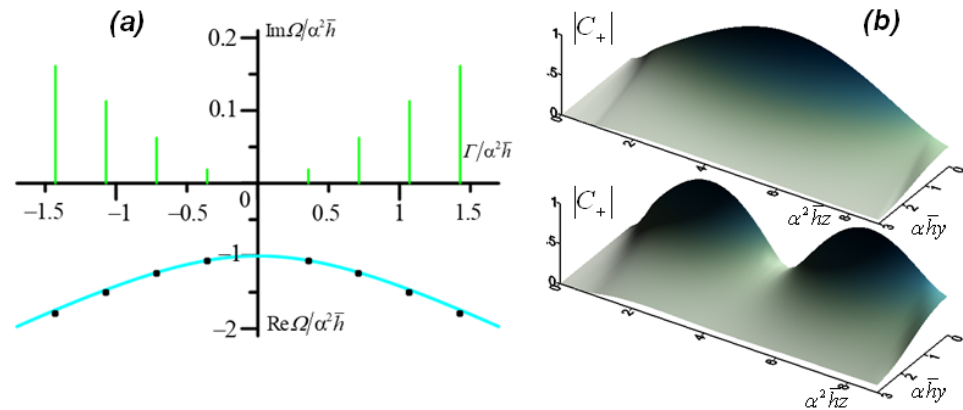


**Figure 8.** (a) Surface wave dispersion curve (solid line) with dots corresponding to mode eigenfrequencies at  $\alpha^2 \bar{h} l_z = 8.8$  in the lower part of the diagram; mode losses are marked by vertical lines in the upper part of the diagram, (b) Spatial profiles of the first two modes of surface-wave resonator.

The mode decrements decrease and Q factors increase with  $L = \alpha^2 \bar{h} l_z$  while the influence of Ohmic losses becomes more significant. We have derived [51], the asymptotic formulas for frequency shifts, Q factors, and mode structures, valid in the case of large length  $L \gg \pi$  and small Ohmic losses  $\sigma/\alpha \sim d_{skin}/b \ll 1$ . The longitudinal structures of high-Q modes resemble those of the closed resonator,

$$C_{\pm}^{(s)}(z, y) \sim \sin \frac{s\pi z}{l_z} e^{-\alpha \bar{h} y} \tag{50}$$

with corresponding frequency shifts (see Figure 8)

$$\text{Re}\Omega_s \approx -c\sqrt{\bar{h}^2 \alpha^4 + \Gamma_s^2} = -c\sqrt{\bar{h}^2 \alpha^4 + \left(\frac{s\pi}{l_z}\right)^2}.$$

The quality factor of the fundamental ( $s = 1$ ) mode can be put down as

$$Q = \frac{1}{Q_{diff}^{-1} + Q_{Ohm}^{-1}}, \tag{51}$$

where

$$Q_{diff} = \frac{L^3}{5\pi^2 \alpha^2} = \frac{\alpha^4 \bar{h}^3 l_z^3}{5\pi^2}; \quad Q_{Ohm} = \frac{1}{2\alpha \bar{h} d_{skin}} \tag{52}$$

are the diffraction Q and the Ohmic Q, correspondingly. The two terms in (52) demonstrate different behavior at the varying parameter  $\alpha$ : while the diffraction term rises as  $Q_{diff} \sim \alpha^4$ , the Ohmic Q decreases as  $Q_{Ohm} \sim \alpha^{-1}$ . This can be explained in a simple way: although the wavebeam coupling rises, the modes become more confined at the corrugation, thus reducing the diffraction losses; at the same time, the less effective the ‘volume’ of the mode, the higher the influence of the Ohmic losses. Thus, there is a distinct maximum in the Q dependence (Figure 9); formulas for the maximum Q and optimum corrugation depth can be found in [51].

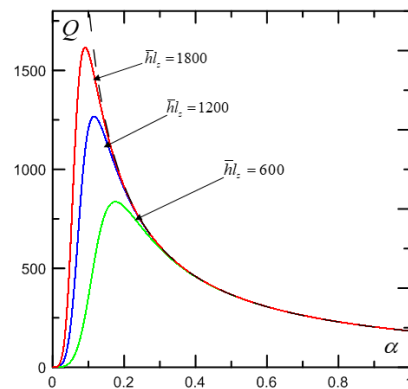


**Figure 9.** Quality factor (51–52) of the fundamental mode of the surface-wave resonator made of copper vs. corrugation depth parameter  $\alpha$  at different values of the system length.

There is an alternative way to find the characteristics of the fundamental mode by simulating the decay process based on time-domain Equations (25) with boundary conditions (48) and initial field distribution  $C_{\pm}|_{t=0} = C_{\pm}^0(y, z)$ . (Figure 10). Obviously, at the initial stage of the simulation, several axial modes are excited. However, after some time, diffraction of the field from the open-edge boundaries leads to the settling of the field distribution which is independent of the initial conditions and corresponds to the formation of the fundamental mode with the highest Q-factor. At this stage (in Figure 10a,  $\omega t > 5000$ ) the wave amplitude decays exponentially in time. The spatial distributions of the partial wave amplitude at the final stage depicted in Figure 10c have a single variation of the field along the  $z$  coordinate and decay exponentially along  $y$  (cf. Equation (50)). All characteristics are in good agreement with those found based on the solution of integral Equation (49). According to the spectrum of the residual radiation at the final stage of simulation presented in Figure 10b, the highest-Q mode has an eigenfrequency of  $\Omega \sim -0.03\bar{h}c$ .

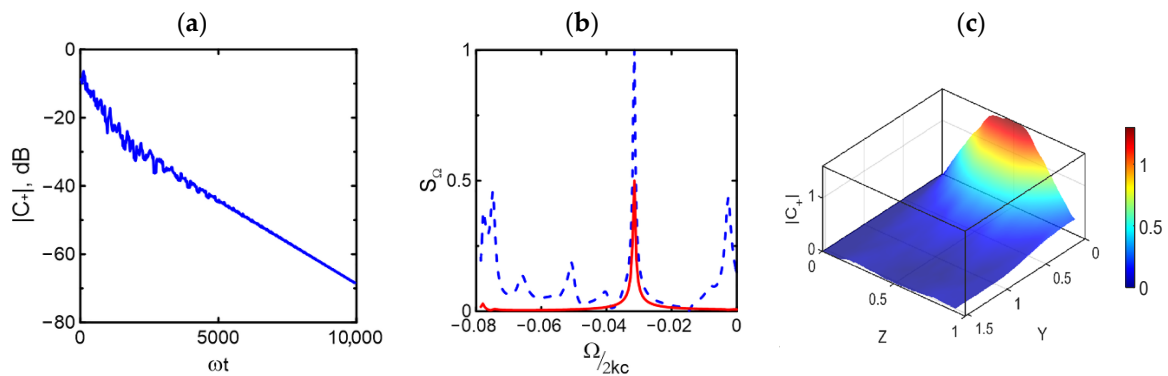


**Figure 10.** Results of simulation of excitation of the highest-Q mode of the surface-wave resonator by initial field distribution at  $\alpha = 1$ : (a) time dependence of the wave amplitudes at the open edge in dB; (b) radiation spectrum at the initial stage of simulation (blue dashed curve) and at the final stage (solid red line); (c) spatial distribution of the forward wave amplitude.

*Cylindrical structures.* The properties of evanescent eigenmodes of corrugated sections of the cylindrical waveguides are similar to those described above. Their discrete mode eigenspectra are characterized beside the two transverse (azimuthal  $m$  and radial  $n$ ) indices and by the third (axial) mode index  $s = 1, 2, 3 \dots$ , which denotes the number of mode field variations along the  $z$  axis. When the criterion (43) is satisfied, high-Q azimuthally symmetric ( $m = 0$ ) evanescent ( $n = 1$ ) eigenmodes are formed in the vicinity of the Bragg frequency (Figure 6).

Similar to the planar case above, using the time-domain Equation (36) we simulate the formation of the fundamental evanescent mode in a section of a cylindrical corrugated

waveguide with a length of  $l_z = 1.75$  cm, mean radius of  $r_0 = 1.5$  mm, corrugation period of  $d = 0.5$  mm, and the amplitude of  $r_1 = 0.075$  mm. Such a system is to be considered further as a slow wave structure for a millimeter-band SWO. In Figure 11b, the oscillation frequency, defined as  $f = (2\pi)^{-1}d(\arg C_+)/dt$ , is shown settling on the fundamental eigenmode (Figure 11a) resembles the one given by Equation (50): it has one variation along the  $z$  axis and decays exponentially in a radial direction.

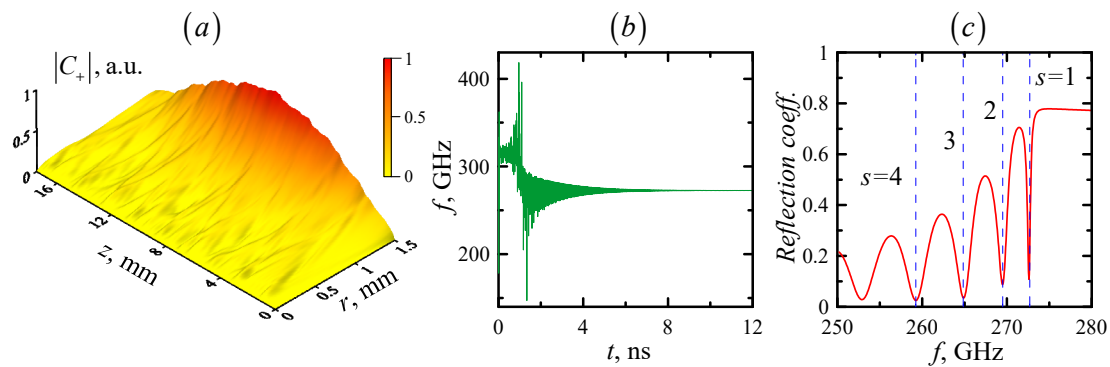


**Figure 11.** Results of simulation of excitation of the corrugated section of the cylindrical waveguide by initial field distribution: (a) spatial distribution of the forward-wave amplitude in the highest-Q mode; (b) instantaneous radiation frequency; (c) Frequency dependence of reflection of incident  $TM_{01}$  mode from corrugated structure: the minima of reflectivity correspond to positions of modes with different axial index  $s$ . Parameters of the periodic structure:  $l_z = 35d$ ,  $d = 0.5$  mm,  $r_0 = 1.5$  mm,  $r_1 = 0.075$  mm.

Note that, similar to planar geometry, high-Q modes with larger axial indices  $s > 1$  exist in the system with eigenfrequencies which lie below the fundamental mode eigenfrequency. These modes are also excited at the initial stage of simulation; however, their Q-factors are lower than those of the fundamental mode, so at the final stage only the fundamental mode remains. Nevertheless, one can recognize the positions of these modes by simulating the reflections of the external  $TM_{01}$  mode of a regular waveguide from the corrugated section. Minima on the frequency dependence of the reflection coefficient can be seen in Figure 11c close to the mode positions, whereas the widths of the dips are reversely proportional to their Q-factors. As shown below in Section 4, higher-index modes can also be excited in the course of beam-wave interaction under Cherenkov synchronism conditions.

### 3. Quasi-Optical Models of Planar Cherenkov-Type Devices

#### 3.1. General Self-Consistent Equations of Electron-Wave Interaction

For a description of radiation sources operation, the wave propagation Equations (8)–(10) (or (33) in case of near-cutoff operation) should include the electron beam current, which is to be found from motion equations for electrons in the field of the corresponding synchronous wave. Consider a relativistic beam (Figure 12) traveling along the corrugated surface, or in the planar waveguide, parallel to the guiding magnetic field with an initial velocity of  $v_{||} = \beta_0 c$ . According to Figure 1, this beam can interact with any of the spatial harmonics  $s$  in the expansion (6) under the Cherenkov synchronism condition (1). For paraxial waves in oversized waveguides, where  $h \approx k = \omega/c$ , Equation (1) yields

$$\omega \approx (k + s\bar{h})v_{||}. \tag{53}$$

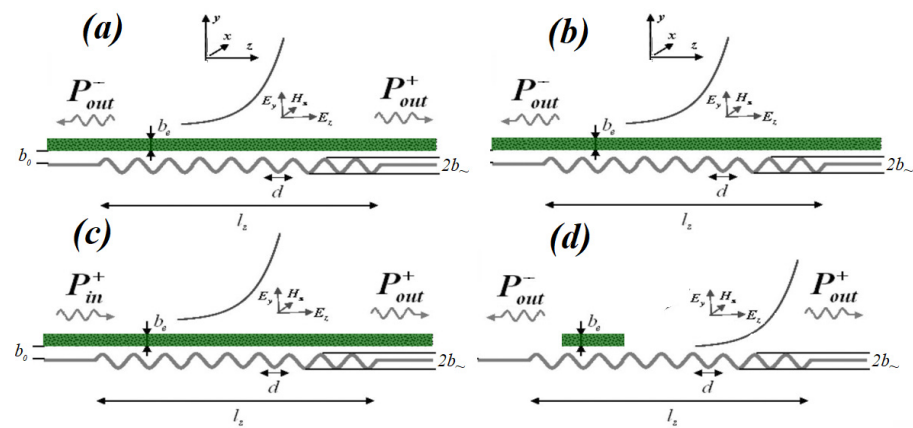


**Figure 12.** Schemes of various Cherenkov-type radiation sources: (a) surface-wave oscillator; (b) backward-wave oscillator; (c) TWT amplifier; (d) super-radiant short-pulse generator.

Similar to Section 2, we limit ourselves to shallow corrugations and cases  $s = 0, \pm 1$ . Under condition (53), the particles are bunched under the action of the electric field component of the corresponding spatial harmonic

$$E_z = -\text{Re} \frac{i}{k} \left[ \left( \frac{\partial H_s}{\partial y} + \frac{4\pi}{c} j_z \right) e^{i(\omega t - (k + s\bar{h})z)} \right] \tag{54}$$

(the second term, in fact, includes the spatial charge field) and is described by equations

$$\frac{d\varepsilon}{dz} = -eE_z; \quad \frac{d\theta}{dz} = \omega \left( \frac{1}{v(\varepsilon)} - \frac{k + s\bar{h}}{\omega} \right), \tag{55}$$

where  $\varepsilon$  and  $v(\varepsilon) = c\sqrt{1 - (\varepsilon/mc^2)^{-2}}$  are the electron’s energy and velocity, and  $\theta = \omega t - (k + s\bar{h})z$  is its phase with respect to the synchronous harmonic. The stationary non-modulated electron beam is described by the boundary conditions set at the entrance of the interaction space

$$\varepsilon_{z=0} = \varepsilon_0, \quad \theta|_{z=0} = \theta_0 \in [0, 2\pi) \tag{56}$$

where  $\varepsilon_0 = mc^2\gamma_0$  and  $\theta_0$  are the initial values of the electron’s energy and phase.

Based on Equations (54) and (55), the non-stationary system of equations describing the interaction between the beam and the  $s$ -th harmonic of the field (6) in the most general form can be formulated as

$$-\frac{(\bar{h} - k)}{k} \frac{\partial H_{-1}}{\partial z} + \frac{1}{c} \frac{\partial H_{-1}}{\partial t} + \frac{i}{2k} \frac{\partial^2 H_{-1}}{\partial y^2} - i \frac{\bar{h}^2 - 2k\bar{h}}{2k} H_{-1} = i\alpha\delta(y)H_0 + i \frac{\partial I^\omega}{\partial y} \delta_{-1,s} \tag{57}$$

$$\frac{\partial H_0}{\partial z} + \frac{1}{c} \frac{\partial H_0}{\partial t} + \frac{i}{2k} \frac{\partial^2 H_0}{\partial y^2} = -i\alpha\delta(y)[H_1 - H_{-1}] + i \frac{\partial I^\omega}{\partial y} \delta_{0,s} \tag{58}$$

$$\frac{k + \bar{h}}{k} \frac{\partial H_1}{\partial z} + \frac{1}{c} \frac{\partial H_1}{\partial t} + \frac{i}{2k} \frac{\partial^2 H_1}{\partial y^2} - i \frac{\bar{h}^2 + 2k\bar{h}}{2k} H_1 = -i\alpha\delta(y)H_0 + i \frac{\partial I^\omega}{\partial y} \delta_{1,s} \tag{59}$$

$$\frac{d\theta}{dz} = \omega \left( \frac{1}{v(\varepsilon)} - \frac{\omega}{k + s\bar{h}} \right), \quad \frac{d\varepsilon}{dz} = \frac{e}{k} \text{Re} \left( i \left( \frac{\partial H_s}{\partial y} - 2kI^\omega \right) e^{i\theta} \right). \tag{60}$$

Here  $\delta_{ij}$  is the Kronecker delta denoting that the beam interacts only with one of the harmonics with index  $s$  ( $s = 0, \pm 1$ ). The excitation factor is  $I^\omega = \frac{2\pi I_0}{kc} \frac{1}{b_e} \psi(y) J$ , where  $\psi(y)$  represents the transverse distribution of electron density, and  $I_0$  is the total beam current,

$$J = \frac{1}{\pi} \int_0^{2\pi} e^{-i\theta} d\theta_0. \tag{61}$$

Equations (57)–(60) constitute a self-consistent system accounting for the non-fixed structure of the field along both the transverse and longitudinal coordinates, unlike the previous models [1–3] describing the electron-wave interaction in Cherenkov O-type devices based on extracting a single waveguide mode with a fixed transverse structure. In this system, the spatial charge forces are taken into account—the corresponding term is in the right-hand part of the motion Equation (60).

Under the assumption of a relatively small  $(\epsilon - \epsilon_0)/\epsilon_0 \ll 1$  variation of the particles' energy, motion equations (56d) can be simplified to the form

$$\left(\frac{\partial}{\partial z} + \frac{1}{v_0} \frac{\partial}{\partial t}\right)^2 \theta = \frac{e\mu}{mc^2\gamma_0} \text{Re} \left( i \left( \frac{\partial H_s}{\partial y} - 2kI^\omega \right) e^{i\theta} \right) \tag{62}$$

where  $\mu = \gamma_0^{-2}\beta_0^{-3}$  is the bunching parameter; the boundary conditions (55) yield

$$\theta|_{z=0} = \theta_0 \in [0, 2\pi), \left. \left( \frac{\partial}{\partial z} + v_{\parallel}^{-1} \frac{\partial}{\partial t} \right) \right|_{z=0} = \Delta, \tag{63}$$

where

$$\Delta = k \left( \frac{1}{\beta_0} - \frac{k}{k + s\bar{h}} \right) \tag{64}$$

is the detuning of the electron's synchronism with the corresponding spatial harmonic at the carrier frequency (for 0th harmonic,  $\Delta = k\beta_0^{-1}(1 - \beta_0)$ , characterizing the difference between the electron velocity and the speed of light and is always positive).

It is expedient to introduce the amplification parameter

$$G = \left( 2\sqrt{2} \frac{eI_0}{mc^3} \frac{\mu}{\gamma_0} \lambda \right)^{\frac{2}{3}}, \tag{65}$$

which is similar to the Pierce parameter [32,33], and normalize the rest of the variables:

$$Z = Gkz, Y = \sqrt{2G}ky, \tau = G\omega_0 t, \hat{\alpha} = \sqrt{\frac{2}{G}}\alpha, \hat{\Delta} = \frac{\Delta}{kG} \tag{66}$$

$$\hat{H}_{\pm 1,0} = \frac{\sqrt{2}e\mu}{mc^2\gamma_0 k G^{3/2}} H_{\pm 1,0}, \Psi(Y) = \psi(y), B_e = \int_0^\infty \Psi(Y) dY. \tag{67}$$

Electron efficiency (relative part of kinetic power in the beam to be converted into radiation) in the stationary oscillation's regime is given by

$$\eta = \frac{G\hat{\eta}}{\mu(1 - \gamma_0^{-1})}, \hat{\eta} = \frac{1}{2\pi B_e} \int_0^B \int_0^{2\pi} \left( \frac{\partial \theta}{\partial Z} - \hat{\Delta} \right) \Big|_{Z=L} \Psi(Y) d\theta_0 dY, \tag{68}$$

where  $L = Gkl_z$  is the normalized length.

### 3.2. Surface-Wave Oscillator in $\pi$ -Mode Operation Regime

At the operation point B in Figure 1 where the radiation frequency is close to the Bragg resonance (17), strong reflections of the forward and backward wavebeams take place at

the corrugated structure described by Equations (57)–(60) for  $s = 0$ , normalized according to (66–67). In this case, it is convenient to choose the Bragg frequency as the carrier one,  $\omega = \bar{h}c/2, k = \bar{h}/2$ ; thus, the  $\bar{h}^2 - 2k\bar{h}$  term in Equations (57)–(60) turns to zero. At the same time, as explained in Section 2.1, the equation for the first harmonic can be dropped. After introducing the symmetric notations  $\hat{C}_+ = \hat{H}_0, \hat{C}_- = \hat{H}_{-1}$  we arrive at equations describing the interaction of two coupled quasi-optical wavebeams (26) with a relativistic electron beam:

$$\begin{aligned} \frac{\partial \hat{C}_+}{\partial Z} + \frac{\partial \hat{C}_+}{\partial \tau} + i \frac{\partial^2 \hat{C}_+}{\partial Y^2} - i \hat{\alpha} \hat{C}_- \delta(Y) + (1 + i) \hat{\sigma} \hat{C}_+ \delta(Y) &= -\frac{i}{B_e} \frac{\partial}{\partial Y} (J\Psi(Y)), \\ -\frac{\partial \hat{C}_-}{\partial Z} + \frac{\partial \hat{C}_-}{\partial \tau} + i \frac{\partial^2 \hat{C}_-}{\partial Y^2} - i \hat{\alpha} \hat{C}_+ \delta(Y) + (1 + i) \hat{\sigma} \hat{C}_- \delta(Y) &= 0, \\ \left( \frac{\partial}{\partial Z} + \beta_0^{-1} \frac{\partial}{\partial \tau} \right)^2 \theta &= \text{Re} \left( \left( \frac{\partial \hat{C}_+}{\partial Y} + \frac{J\Psi(Y)}{B_e} \right) e^{i\theta} \right). \end{aligned} \tag{69}$$

where  $\hat{\sigma} = kd_{skin}/G$  is the normalized Ohmic losses factor (see (25)). In the absence of external energy flows (problem of oscillator self-excitation), Equations (69) should be supplemented by boundary conditions (48) for the waves and (63) for the electron phase with  $\Delta = k\beta_0^{-1}(1 - \beta_0)$ . Equation (61) yields the energy conservation law, which in the stationary oscillation’s regime can be written as

$$\hat{P}_+(Z) + \hat{P}_-(0) + \hat{P}_{Ohm} = 4\hat{\eta}, \tag{70}$$

where  $\hat{P}_\pm = \int_0^\infty |\hat{C}_\pm|^2 dY$  are the normalized power flow densities in  $\pm z$  directions. Note that here power flows in two antiparallel directions are present, which is related to the absolute instability developing in the system. As shown in Section 2.4, the periodical structure in this parameter area acts simultaneously as a slow-wave system and a high-Q Bragg resonator.

Based on Equation (61), we simulated an SWO operating in the sub-mm range ( $\lambda \approx 0.9$  mm) with the electrons’ energy of  $\sim 1$  MeV and a beam current density of 500 A/cm, a distance between the corrugation and the beam of  $b_0 = 0.15$  mm, and a beam width of  $b_e = 0.3$  mm. We chose the following parameters of the slow-wave structure: a period of  $d = 0.5$  mm, a corrugation depth of  $2b_{\sim} = 0.12$  mm, and a system length of  $l_z = 17.5$  mm. The profiles of the excited waves are similar to those obtained in linear electro-dynamical simulations (Figure 10). In Figure 13, typical dependencies of electron efficiency (68) in the process of stationary regime onset are shown in the  $\pi$ -mode excitation regime ( $\gamma_0 = 3.2$ , point B in Figure 1) and at lower energies ( $\gamma_0 = 2.6$ , point C1 in Figure 1 corresponding to BWO regime). The simulations were conducted at two values of the Ohmic losses parameter  $\hat{\sigma}$ . Note that Ohmic losses have almost no influence on the low-energy BWO operation. An increase in the electrons’ energy (and transition to TWT regimes, point A in Figure 1), leads to a dramatic increase in the Ohmic losses effects.

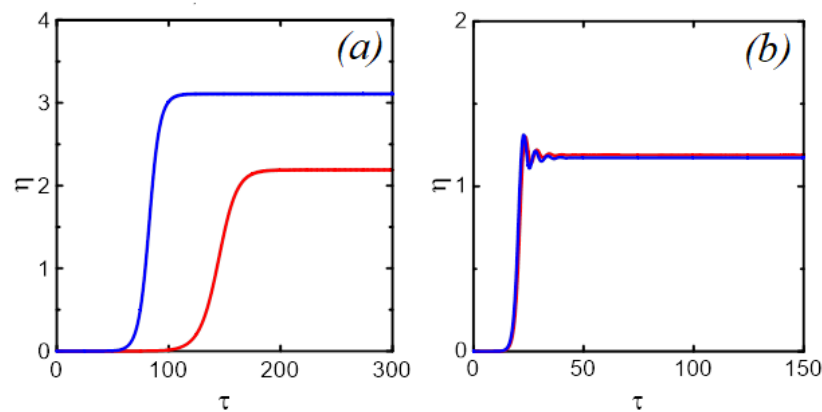


**Figure 13.** Temporal dependencies of normalized electron efficiency at  $\gamma_0 = 3.2$  (a) and at  $\gamma_0 = 2.6$  (b); blue curves correspond to zero Ohmic losses, red curves are plotted for the structure made of copper.

Further, we investigate the dependence of oscillation regimes on the operation point (intersections of the beam line and the dispersion characteristics of the surface wave in Figure 1). Small variations in the initial electrons' energy leads to the displacement of this point from the B position corresponding to a  $\pi$ -mode excitation regime, to the point A area corresponding to a TWT regime (see Section 3.5 below), or C1 corresponding to a BWO regime. For simplicity, we consider zero the Ohmic losses in the optimal regimes close to the BWO area, as their influence is negligibly small. In Figure 14, the dependences of the time increment  $\sigma_t$  and the mismatch of the oscillation frequency from the Bragg resonance  $\Omega = (\omega - \omega_0)/\omega_0$  on the initial electron energy are shown. The red line shows the same mismatch determined by the intersection of the dispersion lines in Figure 1. In Figure 14b, the dependencies of electron efficiency (68) and power densities radiated in  $\pm z$  directions on the beam energy are shown. Oscillations in these dependencies are associated with the excitation of various longitudinal modes found in Section 2.4. This is illustrated by the spatial profiles of the field amplitudes in the stationary oscillation regimes in Figure 14c–h. Note that at decreasing beam energies, the mode structure tends to be BWO-like with the maximum on the cathode side of the interaction space [2].

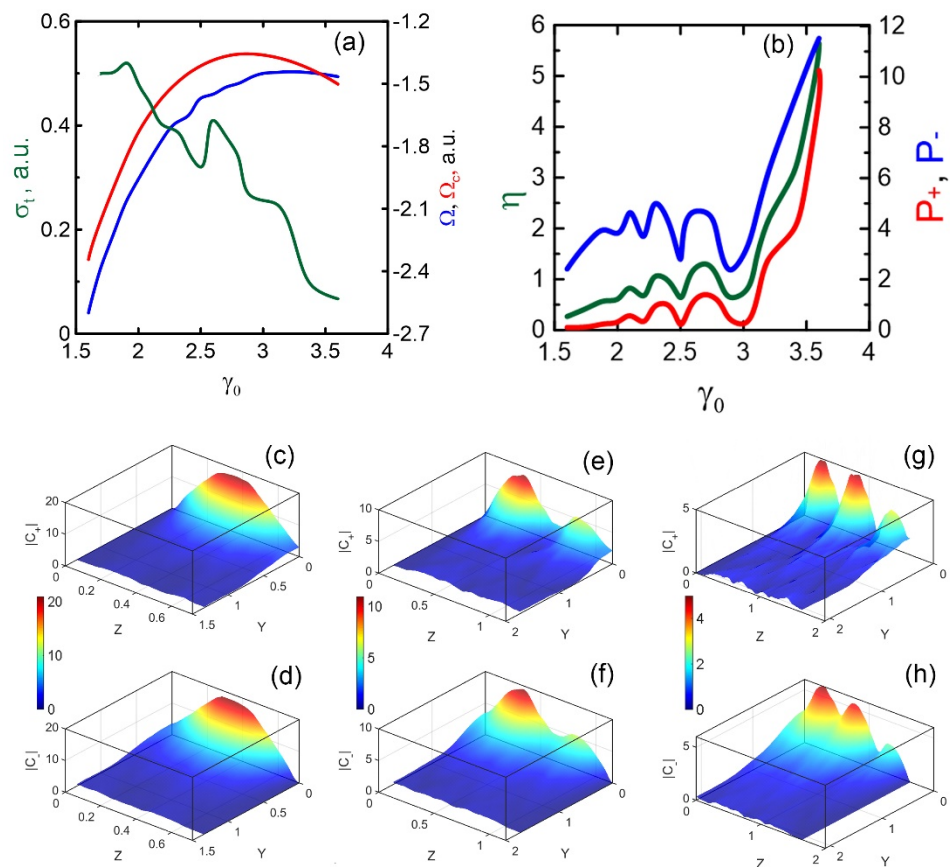


**Figure 14.** Simulations of sub-mm band planar SWO: (a) oscillation frequency (blue), Cherenkov synchronism frequency defined as a frequency of intersection of the beam line and the normal wave characteristic (red); temporal increment (green); (b) electron efficiency (green) and radiation power on the collector (red) and cathode (blue) sides; spatial distributions of partial wavebeam amplitudes: (c,d) bell-shaped structure excited at  $\gamma_0 = 3.2$ ; (e,f) distribution with two variations at  $\gamma_0 = 2.7$ ; (g,h) with three variations at  $\gamma_0 = 2.3$ .

Note that the time increments increase and the starting currents decrease when the synchronism point is shifted to BWO operation (C1 point in Figure 1); however, efficiency drops down (Figure 14b). On the contrary, the efficiency rises in the  $\pi$ -mode and TWT areas (points B and A). The results of the SWO simulations presented in Figure 13a correspond to

point B with a total efficiency of ~10%. The power flow (70) associated with forward wave  $\hat{C}_+$  is about 10 MW/cm, while the one associated with  $\hat{C}_-$  is about 45 MW/cm. We should note that in the  $\pi$ -mode regime, the Ohmic losses reduce the radiation power by 1.5–2 times. The area of the extremum of the dispersion curve (point B) corresponds to the following relation between the system parameters and the energy of ultra-relativistic particles:  $\gamma_* \simeq (2\alpha)^{-1} = d/\pi l_0$ . Further from the exact Bragg resonance (points A and C1), the TWT and BWO regimes are realized, as considered in detail in Sections 3.4 and 3.5, respectively.

### 3.3. Diffraction Mode Selection in the Planar Surface-Wave Oscillator

In Section 3.2, we considered the 2D model of SWO. This model can be generalized to describe the 3D model assuming that the sheet electron beam has a finite width  $l_x^e$  over the  $x$  axis (Figure 1a, insert). The fields here can be presented as (26) and the equations describing the surface-wave excitation are similar to (25) with the equation of electron motion taken into account (transverse coordinate is normalized similar to (66–67),  $X = \sqrt{2Gkx}$ ,  $L_x^e = \sqrt{2Gkl_x^e}$ :

$$\frac{\partial \hat{C}_+}{\partial Z} + \frac{\partial \hat{C}_+}{\partial \tau} + i \frac{\partial^2 \hat{C}_+}{\partial Y^2} + i \frac{\partial^2 \hat{C}_+}{\partial X^2} + (1+i)\sigma \hat{C}_+ \delta(Y) = i\hat{\alpha} \hat{C}_- \delta(Y) - \frac{i}{B_e} \frac{\partial}{\partial Y} (\Psi(X, Y)J), \quad (71)$$

$$- \frac{\partial \hat{C}_-}{\partial Z} + \frac{\partial \hat{C}_-}{\partial \tau} + i \frac{\partial^2 \hat{C}_-}{\partial Y^2} + i \frac{\partial^2 \hat{C}_-}{\partial X^2} + (1+i)\sigma \hat{C}_- \delta(Y) = i\hat{\alpha} \hat{C}_+ \delta(Y), \quad (72)$$

$$\left( \frac{\partial}{\partial Z} + \beta_0^{-1} \frac{\partial}{\partial \tau} \right)^2 \theta = \text{Re} \left[ \left( \frac{\partial \hat{C}_+}{\partial Y} + \frac{J\Psi(X, Y)}{B_e} \right) e^{i\theta} \right], \quad (73)$$

Boundary conditions for Equations (71)–(73) over the longitudinal coordinate  $z$  are given by Equations (48) and (63). In the simulations, we used artificial cyclic conditions (44) over the  $X$ -coordinate which were set at a distance significantly larger than the width of the beam,  $L_x \gg L_x^e$ . Due to the introduction of artificial additional Ohmic losses  $\sigma_{add}$  outside of the beam at  $X > L_x^e/2$  so that  $\sigma_{add}L_x \gg 1$ , the simulation results do not depend on the value of  $L_x$ . We assumed that the beam density is uniform over the transverse cross-section of the beam, i.e.,  $F(X, Y) = 1$  at  $X \in [-L_x^e/2, L_x^e/2]$  and  $Y \in [B_0, B_0 + B_e]$ , where  $B_0 = \sqrt{2Gk}b_0$  is a clearance between the beam and the corrugation surface. The results of the simulations are depicted in Figure 15 for the same corrugation and electron beam parameters as in Section 3.2 for the 2D model.

At a relatively small width of the beam restricted by Fresnel condition  $N_F = l_x^e/4l_z\lambda \leq 1$ , diffraction of radiation in the  $x$ -direction is sufficient for the formation of a regular field structure over this coordinate. In Figure 15b for  $l_x^e = 5 \text{ cm}$  the transverse (over  $x$ ) field structure possesses a regular symmetric distribution (an exponential decay in the  $y$ -direction perpendicularly to the corrugated structure takes place in all variants). For a relatively high electron efficiency of about 10%, the total output power amounts to about 40 MW. For wider beams with  $l_x^e = 10 \text{ cm}$ , multistability regimes take place. For different initial conditions, we observed the excitation of both symmetrical and anti-symmetrical modes. Under the above conditions, a regular symmetric distribution settled in the steady-state regime. With increasing beam width, gains of the first symmetrical and first anti-symmetrical modes (and of all other modes) become very close to each other, thus leading to multistability [39].

Thus, diffraction of radiation in the  $x$ -direction is sufficient for the formation of a regular field. For a wide sheet beam with a large Fresnel parameter  $N_f \gg 1$ , 2D slow-wave structures should be used to provide radiation coherence over transverse coordinates [52,53].

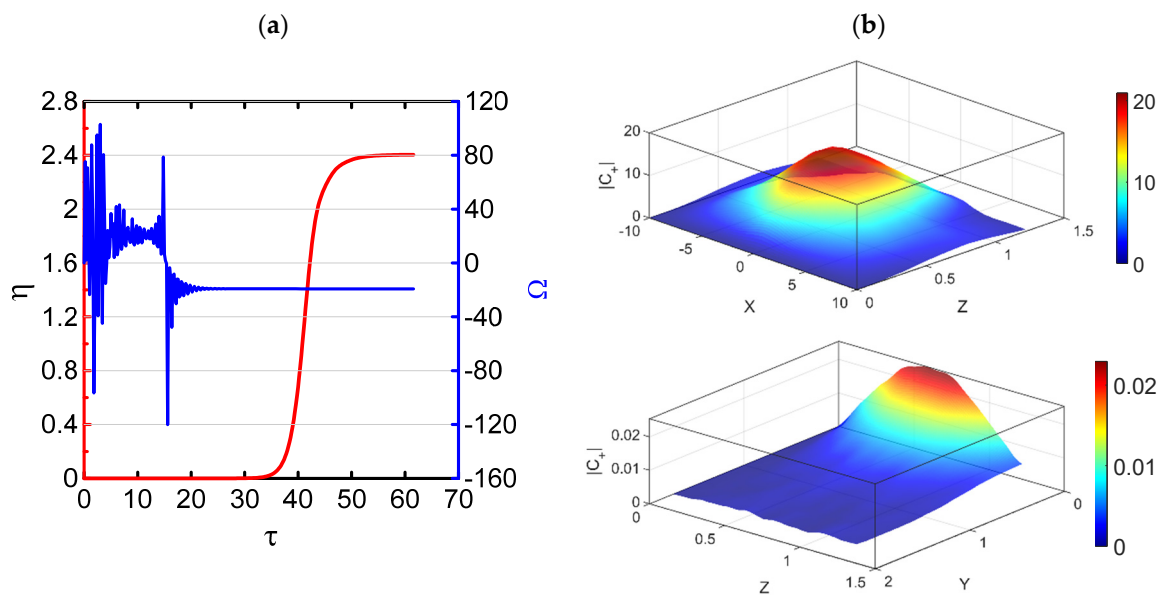


**Figure 15.** Onset of stationary oscillations regime at moderate oversize factor within the 3D model of SWO ( $l_x^e = 5\text{ cm}$ ,  $\gamma_0 = 3.2$ , other parameters are similar to those used in Section 3.2): (a) normalized efficiency (red) and instantaneous frequency (blue) vs. time; (b) spatial structures of the excited field of the forward wave in cross-sections X-Z and Y-Z.

### 3.4. Surface-Wave BWO Operation Regimes

According to Figure 14a, shifting the resonance point in the BWO region with reduced particle energy leads to a decrease in time increments. In this area, the predominant part of the radiation is output from the interaction space with the backward wave  $\hat{C}_-$ . Note the differences in the distribution of the partial wave fields  $\hat{C}_\pm$  in the operation points B and C1 (see Figure 1). At point B, these distributions are close to the structure of the  $\pi$ -type eigenmode formed at the finite-length surface in the absence of the electron beam (Figure 14c,d). In BWO oscillation regimes (C1 point), the partial wave structures are different (Figure 14g,h). The co-propagating partial wave  $\hat{C}_+$  (0th harmonic in terms of Equations (57)–(60)) transforms into a spatial harmonic with an amplitude rapidly decaying along the y-coordinate and proportional to  $\hat{C}_-$  (–1st harmonic), which carries the main energy flow. Further from the Bragg resonance towards point C2 in Figure 1, the two-wave approximation (26) is no longer valid and the amplitude of the –2nd harmonic becomes comparable with that of the 0th harmonic. Thus, at this point it is reasonable to use the three-harmonic Equations (57)–(60) changing the designations of the harmonics (–1st to 0th, 0th to –1st, –2nd to 1st) and the direction of the beam propagation ( $v_{||} \rightarrow -v_{||}$ ). This change means that we choose the operation point C3 instead of C2 in Figure 1; obviously, these points are physically equivalent and differ only in the choice of the direction of the electron’s movement.

At point C3, we use the Equations (57)–(60) with  $s = -1$  describing the beam synchronism with the –1st harmonic corresponding to the Cherenkov BWO operation under condition  $\omega \approx (k - \bar{h})v_{||}$  with  $k < \bar{h}, v_{||} < 0$ . These equations can be simplified in the case when point C3 is far from the Bragg resonance. As shown in Section 2.1, here we can use the impedance approximation and neglect the derivatives with respect to the time and longitudinal coordinate. Using the normalizations (66–67), and introducing  $\hat{\delta}_{\pm 1}^2 = \frac{\bar{h}^2 \pm 2k\bar{h}}{Gk^2}$  we put the system (57–60) to the form

$$\frac{\partial \hat{H}_0}{\partial Z} + \frac{\partial \hat{H}_0}{\partial \tau} + i \frac{\partial^2 \hat{H}_0}{\partial Y^2} = -i \hat{\alpha} \delta(Y) [\hat{H}_1 - \hat{H}_{-1}], \tag{74}$$

$$\frac{\partial^2 \hat{H}_1}{\partial Y^2} - \hat{g}_1^2 \hat{H}_1 = -\hat{\alpha} \delta(Y) \hat{H}_0, \tag{75}$$

$$\frac{\partial^2 \hat{H}_{-1}}{\partial Y^2} - \hat{g}_{-1}^2 \hat{H}_{-1} = \hat{\alpha} \delta(Y) \hat{H} - \frac{1}{B_e} \frac{\partial(\Psi(Y)J)}{\partial Y}, \tag{76}$$

$$\left(\frac{\partial}{\partial Z} - \frac{1}{|\beta_0|} \frac{\partial}{\partial \tau}\right)^2 \theta = \text{Re}\left(i\left(\frac{\partial \hat{H}_{-1}}{\partial Y} + \frac{\Psi(Y)J}{B_e}\right)e^{i\hat{\theta}}\right). \tag{77}$$

The electrons are bunched under the action of the longitudinal component of the electric field of the “−1st” synchronous harmonic. The synchronism detuning (64) in the boundary conditions (63) for the electrons’ motion equations in BWO without a loss of generality can be put to zero. Similarly to Equation (15), we integrate Equation (64) at  $Y > 0$ :

$$\hat{H}_1 = \frac{\hat{\alpha} \hat{H}_0(Y=0)}{\hat{g}_1} e^{-\hat{g}_1 Y}, \tag{78}$$

$$\hat{H}_{-1} = -\frac{\hat{\alpha} \hat{H}_0(0)}{\hat{g}_{-1}} e^{-\hat{g}_{-1} Y} + \frac{1}{2\hat{g}_{-1} B_e} \int_0^\infty \frac{\partial}{\partial Y'} (\Psi(Y')J) \left(e^{-\hat{g}_{-1}|Y-Y'|} + e^{-\hat{g}_{-1}(Y+Y')}\right) dY' \tag{79}$$

Thus, the field of the −1st synchronous spatial harmonic comprises two terms, one of which is induced by the 0th spatial harmonic and is similar to the one (Equation (15)) found in the “cold” problem, whereas the other is associated with the electric current synchronous to the harmonic and its reflection in the perfect conductor. Substituting (78–79) into (74–77), we obtain the equations describing the dynamics of an oversized Cherenkov BWO operating in an SWO regime with a beam synchronous to the −1st harmonic:

$$\frac{\partial \hat{H}_0}{\partial Z} + \frac{\partial \hat{H}_0}{\partial \tau} + i \frac{\partial^2 \hat{H}_0}{\partial Y^2} + i \hat{\chi} \delta(Y) \hat{H}_0 = i \hat{\alpha} \delta(Y) \frac{1}{B_e} \int_0^\infty \Psi(Y') J e^{-\hat{g}_{-1} Y'} dY' \tag{80}$$

$$\left(\frac{\partial}{\partial Z} - \frac{1}{|\beta_0|} \frac{\partial}{\partial \tau}\right)^2 \theta = -\hat{\alpha} \text{Re}\left(i \hat{H}_0(Y=0) e^{i\hat{\theta} - \hat{g}_{-1} Y}\right) + F^q. \tag{81}$$

where  $F^q = \frac{\hat{g}_{-1}}{2B_e} \text{Im}\left\{e^{i\hat{\theta}} \int_0^\infty \Psi(Y') J \left(-e^{-\hat{g}_{-1}|Y-Y'|} + e^{-\hat{g}_{-1}(Y+Y')}\right) dY'\right\}$  is the respective harmonic of the space-charge force taking into account the reflection from the metal [33], and  $\hat{\chi} = \chi \sqrt{2/G}$  is the normalized surface impedance (17) of the corrugated structure.

In the planar waveguide with a second smooth metal wall (Figure 1b), Equations (80) and (81) can be further simplified by the assumption that an electron beam excites a single mode with a fixed transverse structure  $\hat{H}_0(Y, Z) = A(Z) \cos(n\pi Y/B)$  of the fundamental spatial harmonic at the operation point C4 in Figure 1. Under these assumptions, Equations (80) and (81) transform to the form canonical for backward wave oscillators [2]:

$$\frac{\partial \tilde{A}}{\partial Z} + \frac{\partial \tilde{A}}{\partial \tau} + i \tilde{\chi} \tilde{A} = -\frac{1}{B_e} \int_0^{\hat{B}} \Psi(Y) J e^{-\hat{g}_1 Y} dY, \tag{82}$$

$$\left(\frac{\partial}{\partial Z} - \frac{1}{|\beta_0|} \frac{\partial}{\partial \tau}\right)^2 \theta = -\text{Re}\left(\tilde{A} e^{i\hat{\theta} - \hat{g}_1 \hat{Y}}\right) + \tilde{F}^q. \tag{83}$$

Here, the standard normalizations [32] were used instead of (66–67),

$$\begin{aligned} \tilde{Z} &= \left(\frac{2\hat{\alpha}^2}{(1+\delta_{0,n})B}\right)^{1/3} Z = Ckz, \quad \tilde{A} = i\left(\frac{(1+\delta_{0,n})^2 B^2}{4\hat{\alpha}}\right)^{1/3} \hat{A} = i\alpha \frac{\mu}{\gamma_0} \frac{1}{C^2} \frac{eA}{mc^2 k}, \\ \tilde{\chi} &= \left(\hat{\chi} - \frac{2n^2 \pi^2}{(1+\delta_{0,n})B}\right) \left(\frac{(1+\delta_{0,n})B}{2\hat{\alpha}^2}\right)^{1/3}, \quad \tilde{F}^q = F^q \left(\frac{2\hat{\alpha}^2}{(1+\delta_{0,n})B}\right)^{2/3}, \end{aligned}$$

where the Pierce parameter  $C$  is expressed, using (65), as

$$C = \sqrt{\frac{G}{2}} \left(\frac{\alpha^2}{N}\right)^{1/3} = \left(\frac{4\pi e I_0 \mu \alpha^2}{mc^3 k \gamma N}\right)^{1/3}, C = \sqrt{\frac{G}{2}} \left(\frac{4\alpha^2}{N}\right)^{1/3} = \left(\frac{4\pi e I_0 \mu \alpha^2}{mc^3 k \gamma N}\right)^{1/3},$$

$N = kb(1 + \delta_{0,n})/2$  is the norm of the excited mode, and  $\delta_{0,n}$  is the Kronecker delta.

Thus, we demonstrated that the backward partial wave  $\hat{C}_-$  decays relatively slowly along the  $y$  axis according to the deceleration of the fundamental harmonic determined by the impedance function  $\chi(k)$  (see Equation (17)). Oversized planar BWOs were analyzed using Equations (80) and (81) in [47] in application to the experiment currently underway at IAP RAS.

### 3.5. TWT Operation Regimes

*TWT at the fundamental-harmonic ( $s = 0$ ).* Following on from Figure 14, at fairly high electron energies (operation point A in Figure 1) the temporal increment turns to zero. At this point, the absolute instability vanishes; however, the convective instability still takes place. This means that TWT amplifier regimes can be realized. According to Section 2.1, under such conditions the impedance approximation is valid. Neglecting the Ohmic losses for simplicity, assuming that all the processes are monochromatic at the same carrier frequency  $\omega$ , and using Equations (16) and (63), we describe the wave amplification in the fundamental-harmonic TWT by equations [38,41]

$$\frac{\partial \hat{H}_0}{\partial Z} + i \frac{\partial^2 \hat{H}_0}{\partial Y^2} + i \hat{\chi} \delta(Y) \hat{H}_0 = i \frac{1}{B_e} \frac{\partial}{\partial Y} (\Psi(Y) J), \tag{84}$$

$$\frac{\partial^2 \theta}{\partial Z^2} = \text{Re} \left( i \frac{\partial \hat{H}_0}{\partial Y} e^{i\theta} - i \frac{1}{B_e} (\Psi(Y) J) e^{i\theta} \right), \tag{85}$$

$$\theta|_{Z=0} = \theta_0 \in [0, 2\pi), \left. \frac{\partial \theta}{\partial Z} \right|_{Z=0} = \hat{\Delta}. \tag{86}$$

Equations (84) and (85) should be supplemented by the condition for the incident field typical for an amplifier

$$\hat{H}_0(Y, Z = 0) = F_0(Y). \tag{87}$$

The instability increments can be found in the small-signal regime, when perturbations in the electron phase are small,  $\theta = \theta_0 + \vartheta$ ,  $|\vartheta| \ll 1$ , so we can linearize Equation (85), approximate the electron RF current (61) as  $J = -\frac{i}{\pi} \int_0^{2\pi} \vartheta e^{-i\theta_0} d\theta_0$ , and obtain a dispersion equation by presenting the solutions of the linear system  $\sim e^{i\hat{\Gamma}Z - \hat{\xi}Y}$ . In the partial but important case of a thin electron beam  $\Psi(Y) = \delta(Y - B_0)$  moving above the corrugated surface, this equation can be written in the form [38]

$$\left(\hat{\Delta} - \hat{\xi}^2\right)^2 (\hat{\xi} - \hat{\chi}) = -\frac{\hat{\xi}}{2} e^{-\hat{\xi}B_0} \left( (\hat{\xi} + \hat{\chi}) e^{-\hat{\xi}B_0} - (\hat{\xi} - \hat{\chi}) e^{\hat{\xi}B_0} \right). \tag{88}$$

where  $\hat{\xi} = \sqrt{\hat{\Gamma}}$  is the transverse decrement and  $\hat{\Gamma}$  is the normalized amendment to the longitudinal wavenumber  $k$  (cf. Equation (12)). According to coordinate normalizations (66–67), the real longitudinal wavenumber is expressed as

$$h = k(1 + G\hat{\Gamma}) = k(1 + G\hat{\xi}^2). \tag{89}$$

Equations (88) and (89) can be treated as dispersion relations for the interaction of the surface modes, with the electron beam binding the operating frequency  $\omega = kc$  and longitudinal wavenumber  $h$  of the normal waves existing in the system.

Note that due to the interaction with an electron beam, the solutions of Equations (88) and (89) are, generally speaking, complex. The solution corresponding to an amplified evanescent mode has its amplitude  $\hat{H}_0(Y)$  decaying with distance from the beam and its transverse energy flow directed from the beam:

$$\text{Re}\hat{g} > 0 \text{ and } \text{Im}\hat{g} > 0. \tag{90}$$

This mode possesses a positive longitudinal increment  $\text{Im}\hat{\Gamma} = 2\text{Im}\hat{g}\text{Re}\hat{g} > 0$ .

In the dispersion relation (88), beam-wave coupling is governed by  $B_0$  characterizing the distance between the beam and the corrugated surface. At  $B_0 \rightarrow \infty$ , (88) transforms to a factorized fifth-order equation

$$\left( (\hat{\Delta} - \hat{g}^2)^2 - \frac{\hat{\chi}}{2} \right) (\hat{g} - \hat{\chi}) = 0. \tag{91}$$

Since  $\chi$  is purely real, Equation (91) has three solutions with  $\text{Re}g > 0$  and  $\text{Im}g = 0$  corresponding to uncoupled partial waves, namely, a fast and a slow space-charge wave of the modulated electron beam in free space (first factor) and an evanescent wave propagating at the impedance surface (second factor) with a dispersion characteristic  $g(h, k) = \chi(k)$  [38]. The solutions of Equation (91) are depicted in Figure 16 as dashed gray (space-charge waves) and red (evanescent wave) curves. The resonance points of intersection between the space-charge lines and the evanescent wave curve are located in the vicinity of the exact synchronism determined by the relation  $\Delta(k) = \chi^2(k)$ .

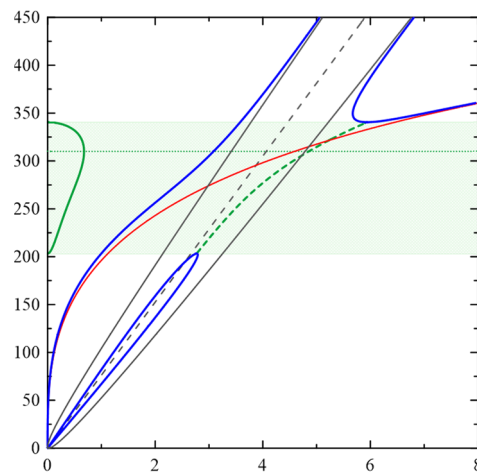


**Figure 16.** Dispersion curves (solid blue lines): frequency vs. longitudinal wavenumber shift. Solid gray and red asymptotes correspond to the partial waves: two space-charge waves and an unperturbed surface wave; dashed gray line is electron’s characteristic  $k = \beta_0 h$ . Green lines denote the frequency dependence of the increment  $\text{Im}h$  (solid line) and wavenumber shift  $\text{Re}h - k$  in the amplification band (shaded area). Dotted line denotes the frequency 310 GHz corresponding to the maximum increment;  $I_0 = 1.2$  kA/cm,  $\gamma = 3$  MV,  $d = 0.25$  mm,  $b_{\sim} = 0.064$  mm, and  $b_0 = 0.5$  mm.

At the finite beam-surface gap  $B_0$ , dispersion curves of the normal waves based on the solutions of Equation (91) are plotted in Figure 16 in blue. Far from the resonance points, they tend to partial wave curves as the coupling decreases. Linear wave interaction mostly takes place in the vicinity of the resonance points as demonstrated by the deflection of normal wave curves from the corresponding asymptotes. A frequency band arises in which two of the roots of Equation (91) become complex and criteria (90) are satisfied for one of them (namely, the one corresponding to the slow space-charge wave). The amplification band (green area in Figure 16) can be a fairly wide-reaching 30% at the parameters specified in the figure caption. The physical reason for such a wide band is the fact that the electrons’

velocity is close to both the phase and group velocities of the surface wave (inclinations of the partial waves' dispersion lines are close to each other at the intersection points).

Full Equations (84)–(87) allow for the description of both the linear and nonlinear stages of interaction and are therefore able to estimate the total electron efficiency, the optimum length of the amplifier, etc. Based on the simulations of the nonlinear regime, we demonstrated the possibility of the realization of a relativistic surface wave amplifier of a submillimeter band with a linear density of incident signal of 50 kW/cm (the master source can be a gyrotron [54]). The blue curve in Figure 17a shows the output power density vs the longitudinal coordinate  $z$  in the maximum increment regime reached at 310 GHz by the parameters given in the Figure 16 caption. Saturation of amplification is reached at a length of about 10 cm with a maximum efficiency of 13.5% and an output power of about 160 MW/cm.

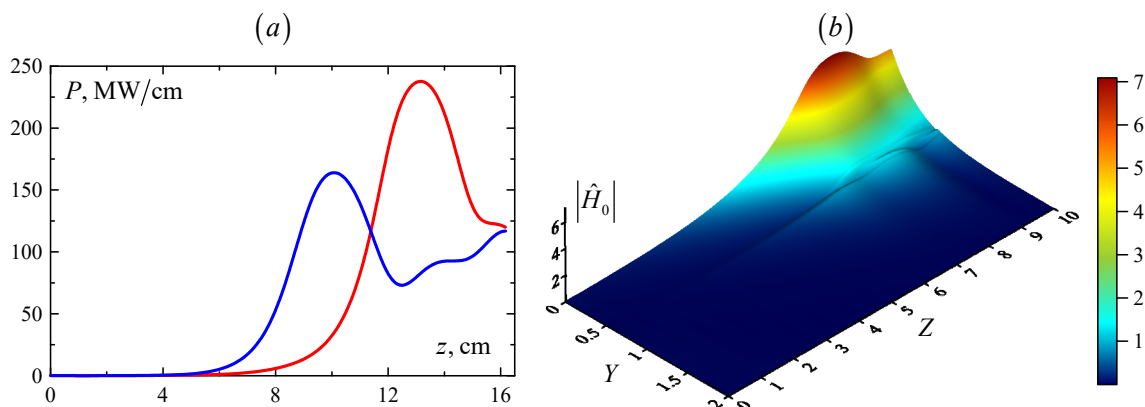


**Figure 17.** Nonlinear stage of beam-wave interaction for physical parameters given in Figure 16 caption. (a) Normalized power of an amplified wave vs. longitudinal coordinate in the optimum-increment regime at 310 GHz (blue curve) and in the maximum-efficiency regime at 330 GHz (red curve). (b) Spatial distribution of the amplified wave amplitude in the latter case.

However, the regime of amplification with a maximum increment turns out not to be optimal in terms of efficiency and output power. Typically for Cherenkov-type microwave amplifiers [32,33], the beam-wave synchronism is sustained longer (thus, the efficiency is larger) in the case of electrons moving slightly faster than the decelerated wave, i.e., at the values of detuning  $\Delta$  smaller than its optimal value determined based on linear theory,  $\Delta < \chi^2$ . In our example, maximum efficiency conditions are satisfied at the frequency of 330 GHz. The red curve in Figure 17a displays the radiated power density vs.  $z$  in the optimal efficiency regime. The optimal interaction length is 13.2 cm, the maximum power density of the amplified signal amounts to 240 MW/cm (total efficiency of 20%), and the gain reaches  $K = 37$  dB. The spatial distribution of the amplified wave is shown in Figure 17b demonstrating that the wave remains confined at the slow-wave system surface.

Presently, relativistic TWTs based on the amplification of surface modes operate in centimeter wavelength bands [17]. According to our analysis [41], at shorter wavelengths such TWTs also appear viable due to the fact that the excitation of evanescent waves provides a regular field pattern over the coordinate normal to the surface, and this solves the transverse mode selection problem inevitable in oversized systems.

*TWT operation at the first spatial harmonic.* For lower beam energies, the beam cannot be synchronous to the fundamental harmonic. However, synchronism is still possible with higher spatial harmonics (operation point D1 in Figure 1). At the 1st harmonic ( $s = 1$ ), when the synchronism condition  $\omega \approx (k + \hbar)v_{||}$  is satisfied and the operation point is far from the Bragg resonance, the amplification of the monochromatic signal can be described by Equations (57)–(60) at  $s = 1$  with normalizations (66–67):

$$\frac{\partial \hat{H}_0}{\partial Z} + i \frac{\partial^2 \hat{H}_0}{\partial Y^2} = -i \hat{\alpha} \delta(Y) [\hat{H}_1 - \hat{H}_{-1}] \tag{92}$$

$$\frac{\partial^2 \hat{H}_1}{\partial Y^2} - \hat{g}_1^2 \hat{H}_1 = -\hat{\alpha} \delta(Y) \hat{H}_0 + \frac{1}{B_e} \frac{\partial}{\partial Y} (\Psi(Y) J) \tag{93}$$

$$\frac{\partial^2 \hat{H}_{-1}}{\partial Y^2} - \hat{g}_{-1}^2 \hat{H}_{-1} = \hat{\alpha} \delta(Y) \hat{H}_0 \tag{94}$$

$$\frac{\partial^2 \theta}{\partial Z^2} = \text{Re} \left( i \left( \frac{\partial \hat{H}_1}{\partial Y} - \frac{\Psi(Y) J}{B_e} \right) e^{i\theta} \right) \tag{95}$$

After the transformations similar to those presented above (Equations (74)–(77) and further), one can reduce Equations (92)–(95) to the form

$$\frac{\partial \hat{H}_0}{\partial Z} + i \frac{\partial^2 \hat{H}_0}{\partial Y^2} + i \hat{\chi} \delta(Y) \hat{H}_0 = i \delta(Y) \frac{\hat{\alpha}}{B_e} \int_0^\infty \Psi(Y') J e^{-\hat{g}_1 Y'} dY'. \tag{96}$$

$$\frac{\partial^2 \theta}{\partial Z^2} = \hat{\alpha} \text{Re} \left[ i \hat{H}_0(0) e^{i\theta - \hat{g}_1 Y} \right] + F^q \tag{97}$$

where  $F^q = \frac{\hat{g}_1}{2B_e} \text{Im} \left\{ e^{i\theta} \int_0^\infty \Psi(Y') J \left( -e^{-\hat{g}_1 |Y - Y'|} + e^{-\hat{g}_1 (Y + Y')} \right) dY' \right\}$  is the space-charge term.

This system should be supplemented with the boundary conditions (86) and (87). Again, in the single-mode planar waveguide, similar to the BWO (Equations (82) and (83)), one can further reduce Equation (76) to a conventional form of TWT equations

$$\frac{\partial \tilde{A}}{\partial Z} + i \tilde{\chi} \tilde{A} = \frac{1}{\tilde{B}_e} \int_0^{\tilde{B}} \Psi(\hat{Y}) J e^{-\hat{g}_1 \hat{Y}} d\hat{Y}, \tag{98}$$

$$\frac{\partial^2 \theta}{\partial Z^2} = \text{Re} \left( \tilde{A} e^{i\theta - \hat{g}_1 \hat{Y}} \right) + \tilde{F}^q. \tag{99}$$

In such approximations, relativistic TWT have been studied in detail in [1].

### 3.6. Orotron Operation Regimes

If the operating point is close to the cutoff frequency of one of the higher modes of the planar waveguide, the orotron [5,26,34,43] regime of interaction is realized. It should be emphasized that the orotron regimes of the Cherenkov interaction exist only in the waveguides; in the case of radiation of an electron beam moving near the corrugated plane into the free space, such a synchronism would correspond to the Smith-Purcell radiation of a pre-bunched beam in the normal direction. For the orotron interaction under a synchronism condition (1) at  $h = 0, s = 1$ , i.e., at  $\omega = \bar{h}v_{||}$  (point D1 in Figure 1), Equation (32) may be rewritten with the inclusion of the electric current similar to (56); after normalizations (66–67), the self-consistent system of orotron equations takes the form:

$$\begin{aligned} \frac{\partial}{\partial \tau} \hat{F}_n + \frac{iG}{2} \frac{\partial^2 \hat{F}_n}{\partial Z^2} &= -i\hat{\alpha} (\hat{H}_1(0, Z) + \hat{H}_{-1}(0, Z)) \\ \frac{\partial \hat{H}_1(y, z)}{\partial Z} + \frac{\partial \hat{H}_1(y, z)}{\partial \tau} + i \frac{\partial^2 \hat{H}_1(y, z)}{\partial Y^2} - i\hat{\delta}_g \hat{H}_1 &= -i\hat{\alpha} \delta(y) \hat{F}_n + \frac{i}{B_e} \frac{\partial}{\partial Y} (\Psi(Y) J) \\ - \frac{\partial \hat{H}_{-1}(y, z)}{\partial Z} + \frac{\partial \hat{H}_{-1}(y, z)}{\partial \tau} + i \frac{\partial^2 \hat{H}_{-1}(y, z)}{\partial Y^2} - i\hat{\delta}_g \hat{H}_{-1} &= -i\hat{\alpha} \delta(y) \hat{F}_n \end{aligned}$$

$$\frac{\partial^2 \theta}{\partial Z^2} = \text{Re} \left( i \left( \frac{\partial \hat{H}_1}{\partial Y} - \frac{\Psi(Y) J}{B_e} \right) e^{i\theta} \right)$$

Here,  $\hat{F}_n = \frac{\sqrt{2e\mu}}{mc^2 \gamma_0 k G^{3/2}} F_n$ ,  $\hat{\delta}_g = \delta_g / kG$  is the normalized geometric mismatch (33) between the Bragg frequency of the propagating partial waves  $\hat{H}_{\pm 1}$  and the cutoff frequency of quasi-

critical mode  $F_n$ . If it is sufficiently large, which is usually the case in orotrons, the time and longitudinal coordinate derivatives can be neglected, similar to Equations (74)–(77):

$$\begin{aligned} \frac{\partial}{\partial \tau} \hat{F}_n + \frac{iG}{2} \frac{\partial^2 \hat{F}_n}{\partial Z^2} &= -i\hat{\alpha}(\hat{H}_1(0, z) + \hat{H}_{-1}(0, z)) \\ \frac{\partial^2 \hat{H}_1(y, z)}{\partial Y^2} - \hat{\delta}_g \hat{H}_1 &= -\hat{\alpha}\delta(y)\hat{F}_n - \frac{1}{B_e} \frac{\partial}{\partial Y}(\Psi(Y)J) \\ \frac{\partial^2 \hat{H}_{-1}(y, z)}{\partial Y^2} - \hat{\delta}_g \hat{H}_{-1} &= -\hat{\alpha}\delta(y)\hat{F}_n \end{aligned} \tag{100}$$

Integrating the last two equations as in Equation (65), we find

$$\hat{H}_{-1} = -\frac{\hat{\alpha}\hat{F}_n}{\sqrt{\hat{\delta}_g}} e^{-\sqrt{\hat{\delta}_g}Y},$$

$$\hat{H}_1 = -\frac{\hat{\alpha}\hat{F}_n}{\sqrt{\hat{\delta}_g}} e^{-\sqrt{\hat{\delta}_g}Y} - \frac{1}{2\sqrt{\hat{\delta}_g}B_e} \int_0^\infty \frac{\partial}{\partial Y'}(\Psi(Y')J) \left( e^{-\sqrt{\hat{\delta}_g}|Y-Y'|} + e^{-\sqrt{\hat{\delta}_g}(Y+Y')} \right) dY'$$

and substitute these expressions into (100) to obtain the time-domain equations of the orotron:

$$\frac{\partial}{\partial \tau} \hat{F}_n + \frac{2i\hat{\alpha}^2 \hat{F}_n}{\sqrt{\hat{\delta}_g}} + \frac{iG}{2} \frac{\partial^2 \hat{F}_n}{\partial Z^2} = i\alpha \frac{1}{B_e} \int_0^\infty \Psi(Y') J e^{-\sqrt{\hat{\delta}_g}Y'} dY' \tag{101}$$

$$\frac{\partial^2 \theta}{\partial Z^2} = -\hat{\alpha} \text{Re} \left[ i\hat{F}_n e^{i\theta - \sqrt{\Delta}Y} \right] + \frac{\sqrt{\hat{\delta}_g}}{2B_e} \text{Im} \left\{ \int_0^\infty \Psi(Y') J \left( e^{-\sqrt{\hat{\delta}_g}|Y-Y'|} + e^{-\sqrt{\hat{\delta}_g}(Y+Y')} \right) dY' \right\} e^{i\theta} \tag{102}$$

A simplified (with no spatial charge taken into account) version of Equations (101) and (102) was used in [33] for the investigation of the dynamic regimes of orotron operation.

### 3.7. Super-Radiant Regimes of Surface-Wave Excitation by Extended Electron Bunches

In recent years, significant progress was made in the generation of short electromagnetic pulses in the centimeter and millimeter wavelength ranges based on the Cherenkov super-radiance (SR) of high-current subnanosecond electron bunches with particle energies of 300–400 keV [55–58] moving in periodically corrugated single-mode waveguides. In these frequency ranges SR pulses of subnanosecond duration with record-breaking gigawatt peak power were obtained by means of “RADAN” and “SINUS 6” compact high-current accelerators [59,60]. The typical duration of bunches employed in these experiments was, on the one hand, large compared to the wavelength and, on the other hand, limited by the so-called coherence length within which the coherent emission of a single electromagnetic pulse from the entire bunch volume is possible due to the slippage of radiation relative to the particles.

A natural continuation of this research is the development of Cherenkov SR sources operating at shorter wavelength values, including the terahertz frequency range [61,62]. In these wavebands, the conditions of ensuring the electron beam transport and reducing Ohmic losses imply the use of oversized (or open) slow-wave systems with surface wave excitation. We describe here the SR regime of surface-wave excitation in the frame of a 3D planar model when an electron bunch with length  $l_z^e$  and width  $l_x^e$  moves over a corrugated surface (Figure 12d)). The excitation factor in the right-hand part of Equation (53) can be presented in the form:

$$j_z^\omega = \frac{qV_0}{V} \psi(z - v_{||}t, x, y) J,$$

where  $q$  is the bunch total charge,  $V = l_z^e l_x^e b_e$  is its volume, and  $\psi$  defines the unperturbed bunch profile. Thus, to describe super-radiant processes, one should use in the right-hand part of Equation (73) the function  $\Psi(Z - \beta_0\tau, X, Y) = \psi(z - v_{||}t, x, y)$ .

In [61], simulations were performed in the terahertz range for an electron bunch with a length of  $l_z^e = 1.2$  cm, transverse dimensions of  $l_x^e = 0.45$  mm and  $b_e = 0.3$  mm, particle energies of 1.5 MeV, and a total bunch charge of 2.2 nC. These parameters can be obtained for the electron bunches generated by photoinjectors [63,64]. The bunch propagated over a plane with a corrugated region of a length of 10 cm, a corrugation period of 0.15 mm, and a corrugation amplitude of 25  $\mu$ m. We used the initial small electron density fluctuations governed by a small parameter as the initial conditions.

The simulations showed that the main fraction of the radiation is emitted in the form of a short SR pulse in the positive direction of the axis  $z$ , i.e., in the direction of propagation of the electron bunch. The temporal dependence of the total radiation power  $P_+ = \int_0^\infty \int_0^\infty |\hat{C}_+(Z=L)|^2 dXdY$  is plotted in Figure 18a. The process of pulse formation is illustrated in Figure 18b–d, where spatial structures of the partial waves are presented. One can see that the amplitudes of both partial waves exponentially decay in the direction of the  $y$  axis with distance from the corrugated surface. In Figure 18, the spatial profiles of the electric field on the cross-section  $Y = 0.6$  are shown in consecutive moments of time (cf. Equation (50)). As seen in the dispersion diagrams, the electron velocity in the resonance point exceeds the group velocity of the surface wave. It leads to the formation of wakefields behind the electron bunch as seen in Figure 18. The peak power of the SR pulse amounted to 3.5 MW at a pulse duration of  $\sim 100$  ps.

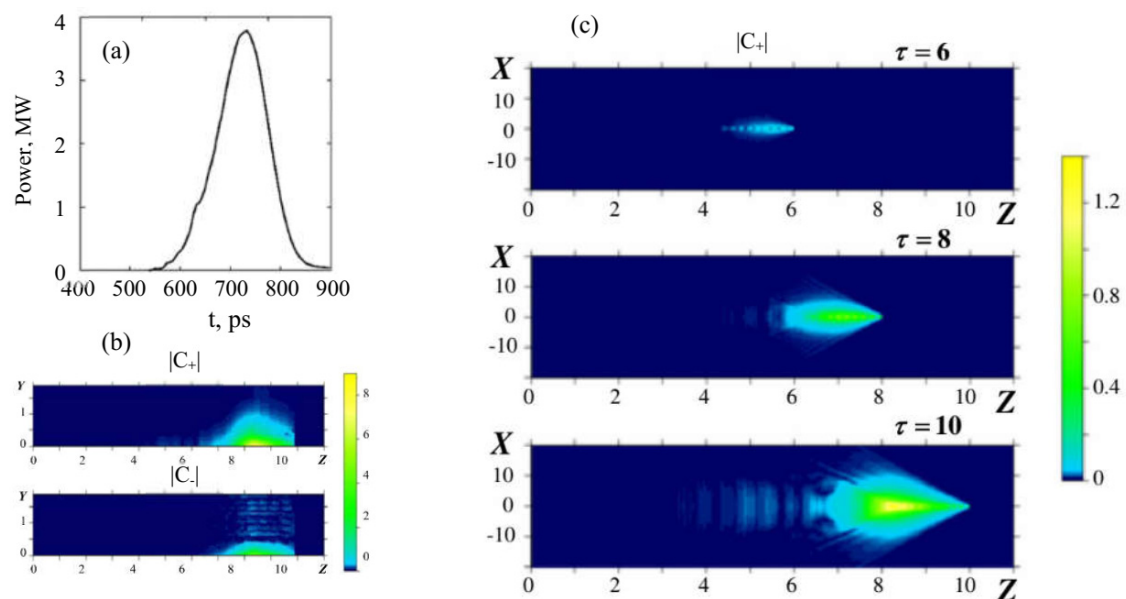


**Figure 18.** (a) SR pulse temporal profile; (b) spatial structures of the partial waves in the cross-section  $X = 0$ ; (c) formation of wake wave after electron bunch: transverse ( $X,Z$ ) profiles of electric field on the surface  $Y = 0.6$  are shown at consecutive points in time.

Note that the excitation of surface waves in the SR regime has been observed experimentally in an oversized cylindrical waveguide where 150 ps SR pulses with a central frequency of 140 THz and a record peak power of 50–70 MW were generated [62].

## 4. Quasi-Optical Theory of Cylindrical Surface-Wave Oscillators

### 4.1. Symmetric Mode Excitation

As mentioned in Section 2.3, most of the experimental realizations of Cherenkov oscillators and amplifiers to date use tubular beams propagating in the cylindrical-geometry interaction spaces. In many of the experiments [18–25], excitation of surface waves was observed. In this section, we analyze the excitation of azimuthally symmetric modes taking into account the non-zero curvature of the waveguide walls, and demonstrate, using the

results of [19] as an example of the simulated values of the starting currents, that output radiation power (etc.) are close to those obtained in the experiment. At the same time, the crucial issue for this class of radiation sources is the problem of limiting oversize factors allowing for the retention of stable oscillations at symmetric modes. We investigate this problem within the quasi-planar model (46).

In SWO with a cylindrical waveguide corrugated according to (34), the excitation of the azimuthally symmetric surface wave by a rectilinear REB are described by time-domain equations derived by including the electric current in Equation (43) [40]:

$$\frac{\partial \widehat{C}_+}{\partial Z} + \frac{\partial \widehat{C}_+}{\partial \tau} + i \frac{\partial}{\partial \rho} \left( \frac{1}{\rho} \frac{\partial (\rho \widehat{C}_+)}{\partial \rho} \right) + i \kappa \widehat{C}_+ + \sigma \delta(\rho - \rho_0) \widehat{C}_+ = i \bar{\alpha} \delta(\rho - \rho_0) \widehat{C}_- + i G \frac{\partial}{\partial \rho} (\psi(\rho) J^e), \quad (103)$$

$$- \frac{\partial \widehat{C}_-}{\partial Z} + \frac{\partial \widehat{C}_-}{\partial \tau} + i \frac{\partial}{\partial \rho} \left( \frac{1}{\rho} \frac{\partial (\rho \widehat{C}_-)}{\partial \rho} \right) + i \kappa \widehat{C}_- + \sigma \delta(\rho - \rho_0) \widehat{C}_- = i \bar{\alpha} \delta(\rho - \rho_0) \widehat{C}_+, \quad (104)$$

$$\frac{du}{dZ} = \text{Re} \left( i \frac{1}{\rho} \frac{\partial (\rho \widehat{C}_+)}{\partial \rho} e^{i\theta} - i G J^e e^{i\theta} \right), \quad \frac{d\theta}{dZ} = u^{-2} + \Delta. \quad (105)$$

The boundary conditions are similar to Equations (48) and (63). Note that the motion Equation (105) is written here in an ultra-relativistic approximation instead of an approximation (62), which allows for describing the regime of significant variation of particle energy and high electron efficiency (compare to Equation (68))

$$\eta = \frac{1}{2\pi \rho_0^2} \int_0^{2\pi} \int_0^{\rho_0} \rho \psi(\rho) (u(L) - 1) d\rho d\theta_0.$$

The following normalizations were used in (80)

$$u = \frac{\gamma}{\gamma_0}, \quad Z = \frac{k_0}{2\gamma_0^2} z, \quad \tau = \frac{\hbar c}{4\gamma_0^2} t, \quad \rho = \sqrt{\frac{k_0 \hbar}{2\gamma_0^2}} r, \quad G = 8\pi \gamma_0 \frac{e I_0}{m_e c^3 k_0^2 B_e}, \quad (106)$$

$$\kappa = \frac{2\gamma_0^2 v_{01}^2}{k_0 \hbar R^2}, \quad \bar{\alpha} = \sqrt{\frac{2}{k_0 \hbar}} \gamma_0 \alpha, \quad \widehat{H}_{\pm} = \frac{e \sqrt{2k_0 \hbar}}{m_e \omega_0^2} H_{\pm}, \quad \Delta = \frac{2\gamma_0^2}{k_0} (k_0 - \hbar/2).$$

In Equations (103)–(105), Ohmic losses are included with a surface impedance  $\sigma = \gamma_0 k_0 d_{sk} (1 + i)/2$ . Equations (103)–(105) describe the nonlinear dynamics of the axially-symmetric model of an SWO under the approximation of non-fixed axial and radial structures of the RF field. The constructed model was verified by simulating the MWCO operation at the parameter values close to those used in the experiment [19] in a 3 cm wavelength band with the parameters presented in Table 1. In the simulations, oscillations settled with an electron efficiency of 24% and an output power of  $P = 0.8$  GW, which is close to the experimental values; field profiles are shown in Figure 19.

**Table 1.** Parameters of 10 GHz band MWCO.

Slow-Wave System Parameters		Electron Beam Parameters	
Length of corrugated section	$l_z = 14$ cm	Total current	$I_0 = 5.8$ kA
Corrugation period	$d = 1.4$ cm	Accelerating voltage	$U = 570$ kV ( $\gamma_0 \approx 2.1$ )
Mean radius	$R = 4.55$ cm ( $R/\lambda \approx 1.5$ )	Mean beam radius	$r_e = 3.7$ cm

Table 1. Cont.

Slow-Wave System Parameters		Electron Beam Parameters	
Corrugation amplitude	$r_{\sim} = 2.93 \text{ mm}$	Beam thickness	$b_e = 3 \text{ mm}$
Output Parameters			
Efficiency	$\eta = 24\%$		
Integral radiated power	$P = 0.8 \text{ GW}$		
Operating frequency	$f = 8.37 \text{ GHz}$		

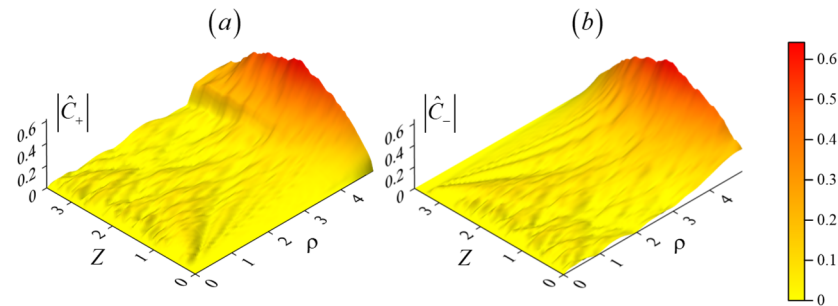


Figure 19. Simulations of 10 GHz MWCO: partial wavebeam amplitudes in stationary oscillation regimes.

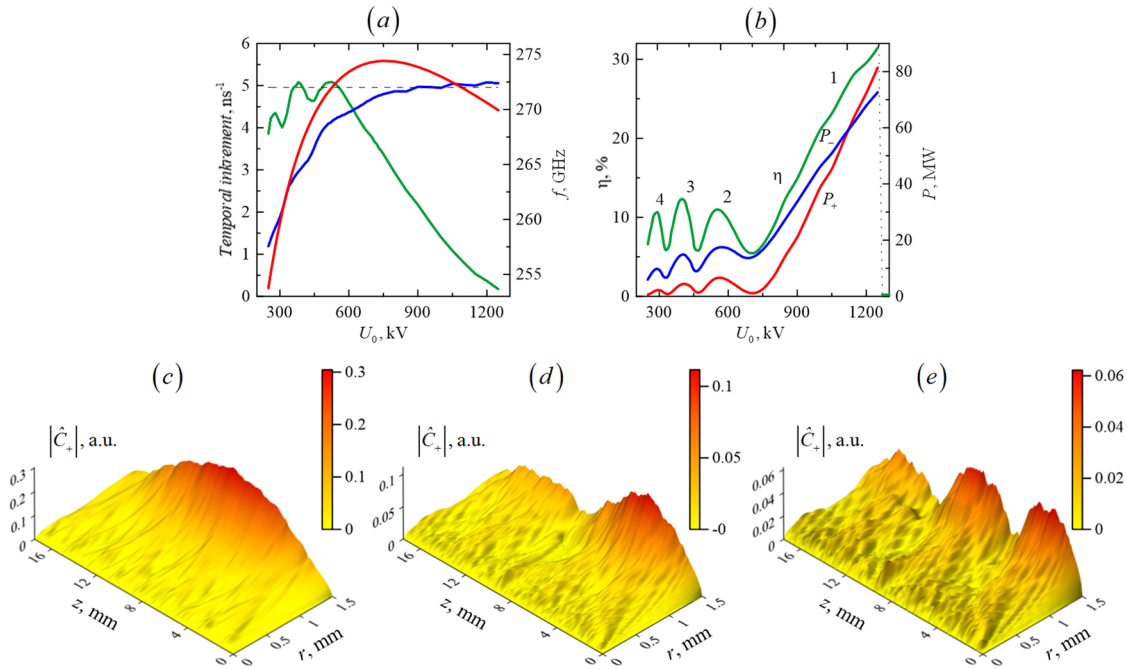
Simulation of 300 GHz-band SWOs. Based on Equations (103-105), we also simulated a millimeter band SWO with the parameters listed in Table 2. Such an SWS satisfies the criterion (43); thus, the slow evanescent wave is present. The synchronism point B in Figure 1c at the top of the evanescent wave curve at 274 GHz corresponds to the voltage of  $U_0 \sim 750 \text{ kV}$ .

Table 2. Parameters of 300 GHz band SWO.

Slow-Wave System Parameters		Electron Beam Parameters	
Length of corrugated section	$l_z = 1.75 \text{ cm}$	Total current	$I_0 = 380 \text{ A}$
Corrugation period	$d = 0.5 \text{ mm}$	Accelerating voltage	$U = 0.3\text{--}1.3 \text{ kV}$
Mean radius	$R = 1.5 \text{ mm} (R/\lambda \approx 1.5)$	Mean beam radius	$r_e = 1.2 \text{ mm}$
Corrugation amplitude	$r_{\sim} = 0.075 \text{ mm}$	Beam thickness	$b_e = 0.3 \text{ mm}$
Output Parameters			
Efficiency	$\eta = 5\text{--}30\%$		
Integral radiated power	$P = 10\text{--}140 \text{ MW}$		
Operating frequency	$f = 264\text{--}273 \text{ GHz}$		

The beam–wave interaction regime in such a system is governed by the accelerating voltage. Single-frequency oscillations were obtained for the range 250–1250 kV as shown in Figure 20. At voltages higher than 1250 kV, the temporal increment (depicted in Figure 20a in green) turns to zero and the oscillations break down. At the voltages 800–1250 kV, a mode close to  $\pi$ -mode with a 272 GHz eigenfrequency (found in Section 2.4) with a single longitudinal variation is generated (Figure 20c). Forward and backward power flows are close in this regime; the electron efficiency is maximized near the oscillation’s breakdown at a voltage of 1250 kV. At lower voltages, the share of power radiated to the collector side decreases and most parts of the radiation are emitted to the cathode side. Local maxima of the efficiency and power in Figure 20b are related to the excitation of higher-order axial modes. Their frequencies are close to the eigenfrequencies of the axial modes depicted in Figure 11e. Accordingly, the established field has two longitudinal variations at 550 kV,

three at 400 kV, four at 300 kV, etc. Similar to the planar case considered in Section 3.2, the field structures presented in Figure 20c–e show that at lower voltages, the field profiles tend to a BWO-like structure with an amplitude maximum shifted to the cathode side [2]. The oscillation frequency (blue line) tends to the frequency of the exact Cherenkov synchronism with the evanescent mode, shown as a red curve. The maximum of the temporal increment corresponding to the minimum starting current is shifted to the BWO side from the top of the normal wave dispersion curve.



**Figure 20.** Simulations of mm band SWO with various acceleration voltages: (a) oscillation frequency (blue), Cherenkov synchronism frequency defined as a frequency of intersection of the beam line and the normal wave characteristic (red), eigenfrequency of the highest-Q mode is marked by a black dashed line; temporal increment (green); (b) electron efficiency (green) and radiation power on the collector (red) and cathode (blue) sides; spatial distributions of the forward wavebeam amplitude: bell-shaped structure with a single axial variation (c) excited at the accelerating voltage of 1200 kV; distribution with two variations (d) at 550 kV; with three variations (e) at 400 kV.

#### 4.2. Non-Symmetric Mode Excitation

Here, we study the problem of increasing the oversize while retaining stable operation at the symmetric modes. As shown in Section 2.3, at the waveguide radiuses are much larger than the wavelength  $R \gg \lambda$ , a local system of coordinates can be introduced at the waveguide surface,  $z = z, y = (R - r)$  so the surface can be considered quasi-planar. The formation of the azimuthal structure of the field is then described by Equations (71)–(73) with the transverse (azimuthal) coordinate  $X = -\sqrt{2GR}\varphi$ . For the tubular electron beam  $\Psi(X) = \text{const}$ , and the cylindrical geometry is taken into account by the cyclicity condition (44), which allows for the expansion of the solutions into the Fourier series (45). With the inclusion of an HF electric current, the equations for competing azimuthal modes in normalizations (66–67), take the form [39]:

$$\begin{aligned} \frac{\partial \hat{C}_+^m}{\partial Z} + \frac{\partial \hat{C}_+^m}{\partial \tau} + i \frac{\partial^2 \hat{C}_+^m}{\partial Y^2} + iP^2 m^2 \hat{C}_+^m &= i \hat{\alpha} \hat{C}_-^m \delta(Y) - \frac{1}{B_e} \frac{\partial J_m}{\partial Y}, \\ -\frac{\partial \hat{C}_-^m}{\partial Z} + \frac{\partial \hat{C}_-^m}{\partial \tau} + i \frac{\partial^2 \hat{C}_-^m}{\partial Y^2} + iP^2 m^2 \hat{C}_-^m &= i \hat{\alpha} \hat{C}_+^m \delta(Y), \\ \left( \frac{\partial}{\partial Z} + \beta_0^{-1} \frac{\partial}{\partial \tau} \right)^2 \theta &= \text{Re} \sum_{m=-\infty}^{\infty} \left[ \frac{\partial \hat{C}_+^m}{\partial Y} e^{i(\theta+mPX)} \right], \end{aligned} \tag{107}$$

where  $J_m = \frac{2}{\pi L_x B_e} \int_0^{L_x} \int_0^{2\pi} \Psi(Y) e^{-imPX} e^{-i\theta} dXd\theta_0$  is the electron current,  $P = 2\pi/L_x$ , and  $L_x = 2\pi GkR$  is the normalized perimeter of the waveguide. It should be noted that in (107), initially non-interacting azimuthal modes (45) are involved in the non-linear competition process due to interaction with the electron beam.

Figure 21 shows the results of the simulation of azimuthal mode competition in the 10 GHz MWCO [19] at the waveguide radius used in the experiment,  $R = 4.55$  cm. The initial conditions were set as small “seed” values, equal for every mode. For azimuthally-nonsymmetric modes, the increment for a given oversize factor is much less than that of the symmetric mode. As a result, these modes are suppressed at the non-linear competition stage, and the stationary oscillation regime takes place with the excitation of the symmetric mode. At an enlarged system radius, although the current density is retained, increments of different azimuthal modes become closer. Nevertheless, azimuthally symmetric mode still wins in the case of equal initial conditions for every mode. However, if we set the non-zero initial condition only for the mode with  $m = 1$ , the stationary regime at this mode would be settled, thus demonstrating the multistability of MWCO operation. A further increase in the oversize factor leads to oscillations at non-symmetric modes even with equal initial conditions, as shown in Figure 21b at  $R = 22.5$  cm. The stability of the single-mode operation regime can be ensured by using the 2D periodical structures [52–54].

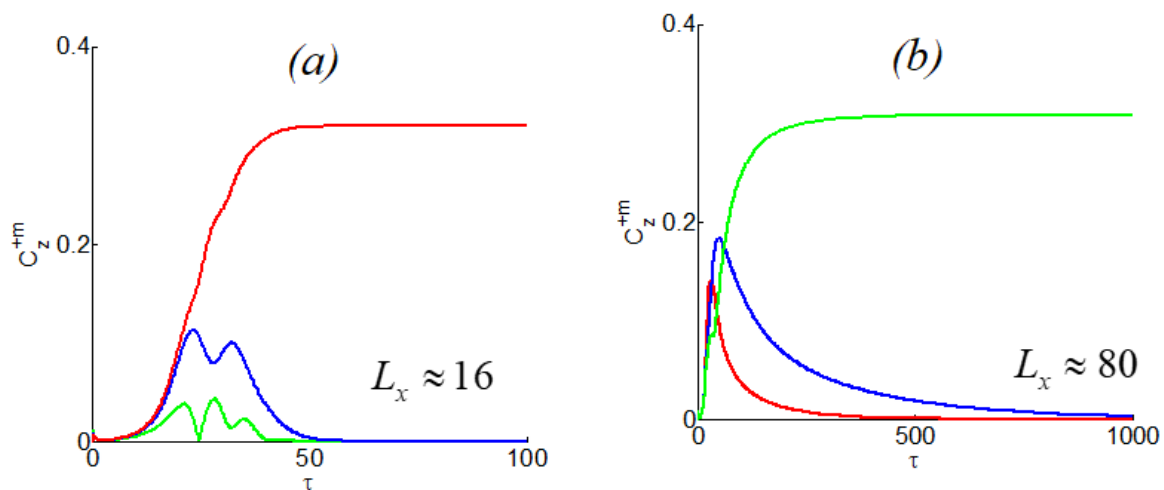


**Figure 21.** Simulation of the nonlinear multimode dynamics of 10 GHz MWCO: mode amplitudes with different azimuthal indexes (red:  $m = 0$ , blue:  $m = 1$ , green:  $m = 2$ ) at (a)  $L_x = 16$ ; (b)  $L_x = 80$ . Initial conditions for all modes are identical.

### 5. Conclusions—Novel Schemes of Relativistic Surface-Wave Devices Utilizing Complex Gratings

Thus, the quasi-optical theory of relativistic Cherenkov devices proved to be a valuable and reliable instrument for the analysis and optimization of most of the generators and amplifier schemes based on synchronous interaction of rectilinear electron beams with waves propagating near shallowly corrugated metal plates. Not only does it provide a means for simulation of oversized systems using reasonable computer resources (as an alternative to direct PIC solvers involving full non-averaged Maxwell equations and simulation of numerous particles’ motion), but it gives a researcher a deep and thorough understanding of the mechanisms of electron-wave interaction in these devices.

Even more importantly, both from practical and fundamental points of view, quasi-optical theory as presented above can easily be modified to propose novel variants of devices, thus solving many of the inherent problems of traditional Cherenkov-type sources. Primarily, this applies to exploiting complex (compared to conventional single-periodic corrugations) gratings involving coupling with additional wavebeams.

First of all, we should mention that SWOs with 2D corrugated structures (Figure 22a,b) provide coupling of the four wavebeams (cf. Equation (26)). Two of them, similar to 1D systems, propagate parallel to the REB, whereas the other two are directed in a transverse direction with respect to the electrons' velocity. These additional wavebeams synchronize the radiation of wide sheet or tubular electron beams allowing for an increase of the REB transverse size along the transverse ( $x$ ) coordinate. Thus, it is possible to increase the total radiated power while maintaining the spatial coherence of radiation. Earlier, such an approach was implemented in free electron masers with 2D distributed feedback [65,66]. In fact, in [53] we have shown that it can be applied to Cherenkov-type devices when the 2D periodic structure is simultaneously a slow-wave system and a 2D Bragg resonator. The operability and efficiency of Cherenkov oscillators with 2D structures were demonstrated experimentally in the Ka-band with MW radiation output power [67]. Even more impressive are the experiments with Cherenkov super-radiant emissions in 2D corrugated structures [68], in which subnanosecond 90 GHz SR pulses with a record-level peak power of up to 150 MW and an axially symmetric directional pattern were generated.

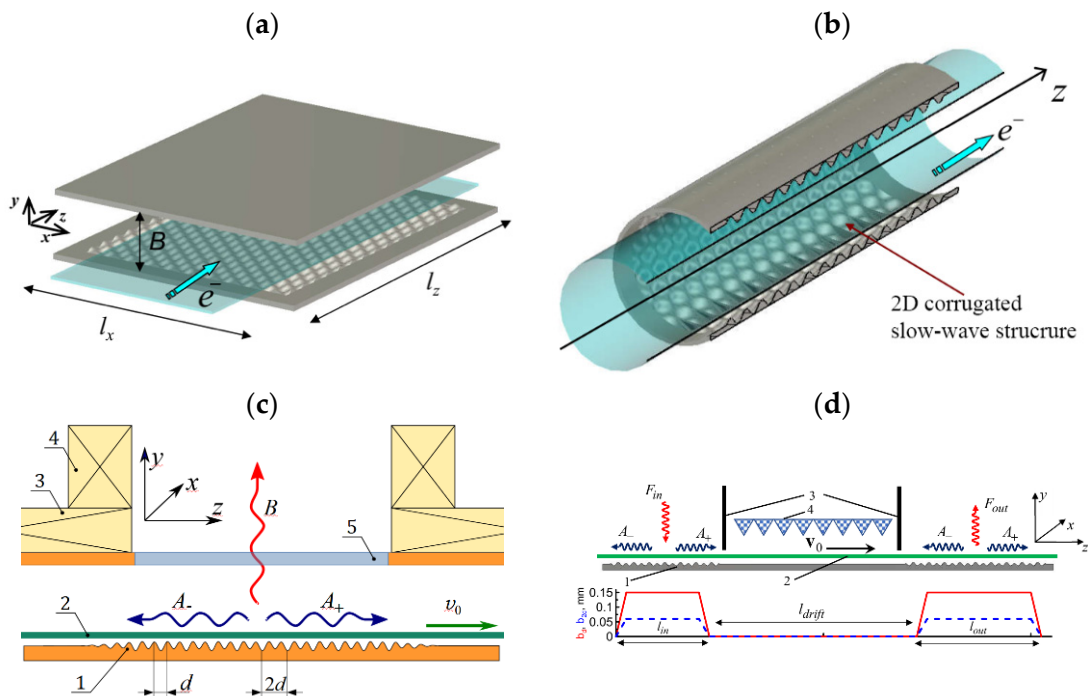


**Figure 22.** Novel schemes of relativistic surface-wave oscillators with complex slow-wave structures. (a) Planar and (b) cylindrical relativistic surface-wave oscillators with two-dimensional periodic gratings. Additional transverse (lateral) propagating wavebeams synchronize the emission from the wide sheet or annular rectilinear electron beam. (c) Surface-wave oscillator with transverse energy output 1: slow-wave structure with additional subharmonics, providing coupling of paraxial wavebeams  $A_+$  and  $A_-$  with transverse wavebeam  $B$ ; 2: rectilinear relativistic electron beam; 3: solenoid; 4: auxiliary Helmholtz coils; 5: output window. (d) Surface-wave EIK-amplifier with transverse energy input and output. 3: Diaphragms separating the drift region, 4: absorber.

Another illustration of the efficacy of the quasi-optical approach is the proposal for the organization of the transverse (in this case, in the normal direction to the corrugated surface) radiation output of the relativistic SWOs [69]. This can be achieved by implementing the additional subharmonic (with a period twice the size of the period of the lattice forming the surface wave) corrugation (Figure 22c). In this case, the output radiation pattern would be Gaussian-like. On the one hand, this leads to the problem of converting the surface wave into the bulk mode of the output waveguide. On the other hand, the Ohmic losses and the losses associated with the propagation of radiation into the cathode side

are dramatically decreased in such a scheme. It should also be noted that such complex lattices can also be used for the input of radiation into the system and the excitation of the surface wave. Spatially divided lattices of the input and output sections can be used for the implementation of amplification devices (Figure 22d), which can be considered to be the variants of the extended interaction klystrons [70].

**Author Contributions:** Conceptualization, N.G. and A.M.; methodology, A.M. and A.S.; software, A.S.; formal analysis, A.M. and I.Z.; investigation, A.M., I.Z., and V.Z.; data curation, I.Z. and V.Z.; writing—original draft preparation, A.M.; writing—review and editing, N.G.; visualization, A.M., I.Z. and V.Z.; supervision, N.G. All authors have read and agreed to the published version of the manuscript.

**Funding:** This research was funded by the Complex DETR Program through IAP RAS (Grant Number: 0030-2021-0027).

**Data Availability Statement:** Data is contained within the article.

**Acknowledgments:** The authors are grateful to A.E. Fedotov, I.V. Zotova, and N.S. Peskov for their stimulating discussions.

**Conflicts of Interest:** The authors declare no conflict of interest.

## References

1. Kovalev, N.F.; Petelin, M.I.; Raiser, M.D.; Smorgonskii, A.V.; Tsopp, L.E. Generation of powerful electromagnetic radiation pulses by a beam of relativistic electrons. *JETP Lett.* **1973**, *18*, 138.
2. Kovalev, N.F.; Petrukhnina, V.I.; Smorgonskii, A.V. Ultrarelativistic carcinotron. *Radio Eng. Electron. Phys.* **1975**, *20*, 1547–1550. (In Russian)
3. Kovalev, N.F.; Smorgonsky, A.V. The theory of ultrarelativistic TWT. *Radio Eng. Electron. Phys.* **1975**, *20*, 1305–1309. (In Russian)
4. Carmel, Y.; Ivers, J.; Kribel, R.E.; Nation, J.A. Intense Coherent Cherenkov Radiation Due to the Interaction of a Relativistic Electron Beam with a Slow-Wave Structure. *Phys. Rev. Lett.* **1974**, *33*, 1275. [[CrossRef](#)]
5. Bratman, V.L.; Denisov, G.G.; Kol'chugin, B.D.; Korovin, S.D.; Polevin, S.D.; Rostov, V.V. Powerful millimeter-wave generators based on the stimulated Cerenkov radiation of relativistic electron beams. *Int. J. Infrared Millim. Waves* **1984**, *5*, 1311–1332. [[CrossRef](#)]
6. Bratman, V.L.; Denisov, G.G.; Ofitserov, M.M.; Korovin, S.D.; Polevin, S.D.; Rostov, V.V. Millimeter-wave HF relativistic electron oscillators. *IEEE Trans. Plasma Sci.* **1987**, *15*, 2–15. [[CrossRef](#)]
7. Abe, D.K.; Carmel, Y.; Miller, S.M.; Bromborsky, A.; Levush, B.; Antonsen, T.M., Jr.; Destler, W.W. Experimental Studies of Overmoded Relativistic Backward-Wave Oscillators. *IEEE Trans. Plasma Sci.* **1998**, *26*, 591–604. [[CrossRef](#)]
8. Levush, B.; Antonsen, T.M.; Bromborsky, A.; Lou, W.R.; Carmel, Y. Relativistic backward-wave oscillators: Theory and experiment. *Phys. Fluids B* **1992**, *4*, 2293. [[CrossRef](#)]
9. Gunin, A.V.; Klimov, A.I.; Korovin, S.D.; Kurkan, I.K.; Pegel, I.V.; Polevin, S.D.; Roitman, A.M.; Rostov, V.V.; Stepchenko, A.S.; Totmeninov, E.M. Relativistic X-band BWO with 3-GW output power. *IEEE Trans. Plasma Sci.* **1998**, *26*, 326–331. [[CrossRef](#)]
10. Abubakirov, E.B.; Denisenko, A.N.; Kovalev, N.F.; Kopelovich, E.A.; Savel'ev, A.V.; Soluyanov, E.I.; Fuks, M.I.; Yastrebov, V.V. Relativistic backward wave oscillator using a selective mode converter. *Tech. Phys.* **1999**, *44*, 1356–1359. [[CrossRef](#)]
11. Kovalev, N.F.; Palitsin, A.V.; Fuks, M.I. Cyclotron Suppression of Generation in a Relativistic Backward-wave Oscillator of Cherenkov Type. *Radiophys. Quantum Electron.* **2006**, *49*, 93–107. [[CrossRef](#)]
12. Moreland, L.D.; Schamiloğlu, E.; Lemke, R.W.; Roitman, A.M.; Korovin, S.D.; Rostov, V.V. Enhanced frequency agility of high-power relativistic backward wave oscillators. *IEEE Trans. Plasma Sci.* **1996**, *24*, 852–858. [[CrossRef](#)]
13. Goykhman, M.B.; Kladukhin, V.V.; Kladukhin, S.V.; Kovalev, N.F.; Kolganov, N.G.; Khramtsov, S.P. A high power relativistic backward wave oscillator with a longitudinal slot slow-wave system. *Tech. Phys. Lett.* **2014**, *40*, 84–86. [[CrossRef](#)]
14. Totmeninov, E.M.; Klimov, A.I.; Rostov, V.V. Relativistic Cherenkov microwave oscillator without a guiding magnetic field. *IEEE Trans. Plasma Sci.* **2009**, *37*, 1242–1245. [[CrossRef](#)]
15. Bunkin, B.V.; Gaponovgrekhov, A.V.; Elchaninov, A.S.; Zagulov, F.Y.; Korovin, S.D.; Mesyats, G.A.; Osipov, M.L.; Otlivanchik, E.A.; Petelin, M.I.; Prokhorov, A.M.; et al. Radar based on UHF-generator with relativistic electron-beam. *Pisma V Zhurnal Tekhnicheskoi Fiz.* **1992**, *18*, 61–65.
16. Abubakirov, E.B.; Botvinnik, I.E.; Bratman, V.L.; Vinogradov, D.V.; Denisov, G.G.; Kazacha, V.I.; Krasnykh, A.K.; Ofitserov, M.M.; Perelstein, E.A.; Sidorov, A.I. Generation of Powerful UHF Emission of Millimeter-wave Range in the Cherenkov TWT with Relativistic High-current Electron-beams. *Zhurnal Tekhnicheskoi Fiz.* **1990**, *60*, 186–190. (In Russian)
17. Abubakirov, E.B.; Denisenko, A.N.; Fuchs, M.I.; Kolganov, N.G.; Kovalev, N.F.; Petelin, M.I.; Savelyev, A.V.; Schamiloğlu, E.; Soluyanov, E.I.; Yastrebov, V.V. An X-band gigawatt amplifier. *IEEE Trans. Plasma Sci.* **2002**, *30*, 1041–1052. [[CrossRef](#)]

18. Alexandrov, A.F.; Galuzo, S.Y.; Kanavets, V.I.; Pletyushkin, V.A. Surface wave excitation by electron flow in a diaphragmatic waveguide. *Sov. J. Tech. Phys.* **1981**, *51*, 1727–1730.
19. AVlasov, N.; Shkvarunets, A.G.; Rodgers, J.C.; Carmel, Y.; Antonsen, T.M.; Abuelfadl, T.M.; Lingze, D.; Cherepenin, V.A.; Nusinovich, G.S.; Botton, M.; et al. Overmoded GW-class surface-wave microwave oscillator. *IEEE Trans. Plasma Sci.* **2000**, *28*, 550–560.
20. Bugaev, P.S.; Cherepenin, V.A.; Kanavets, V.I.; Klimov, A.I.; Kopenkin, A.D.; Koshelev, V.I.; Popov, V.A.; Slepko, A.I. Relativistic multiwave Cherenkov generators. *IEEE Trans. Plasma Sci.* **1990**, *18*, 525–536. [[CrossRef](#)]
21. Wang, G.; Wang, J.; Tong, C.; Li, X.; Wang, X.; Li, S.; Lu, X. A repetitive 0.14 THz relativistic surface wave oscillator. *Phys. Plasmas* **2013**, *20*, 043105. [[CrossRef](#)]
22. Wang, G.; Wang, J.; Zeng, P.; Li, S.; Wang, D. Overmoded Subterahertz Surface Wave Oscillator with Pure TM<sub>01</sub> Mode Output. *Phys. Plasmas* **2016**, *23*, 023104. [[CrossRef](#)]
23. San, M.T.; Ogura, K.; Yambe, K.; Annaka, Y.; Gong, S.; Kawamura, J.; Miura, T.; Kubo, S.; Shimozuma, T.; Kobayashi, S.; et al. Experimental Study on W-Band (75–110 GHz) Oversized Surface Wave Oscillator Driven by Weakly Relativistic Electron Beams. *Plasma Fusion Res.* **2016**, *11*, 2406085. [[CrossRef](#)]
24. Wang, J.; Wang, G.; Wang, D.; Li, S.; Zeng, P. A megawatt-level surface wave oscillator in Y-band with large oversized structure driven by annular relativistic electron beam. *Sci. Rep.* **2018**, *8*, 6978. [[CrossRef](#)] [[PubMed](#)]
25. Li, S.; Wang, J.; Wang, D. Relativistic Surface Wave Oscillator in Y-Band with Large Oversized Structures Modulated by Dual Reflectors. *Sci. Rep.* **2020**, *10*, 336. [[CrossRef](#)] [[PubMed](#)]
26. Rusin, F.S.; Bogomolov, G.D. Generation of Electromagnetic Oscillations in an Open Resonator. *JETP Lett.* **1966**, *4*, 160.
27. Asgekar, V.B.; Dattoli, G. Theory Of Cherenkov Free Electron Lasers: An Analytical Treatment of Saturation. *Opt. Commun.* **2005**, *255*, 309. [[CrossRef](#)]
28. Ginzburg, N.S.; Kuznetsov, S.P.; Fedoseeva, T.N. Theory of transients in relativistic backward-wave tubes. *Radiophys. Quantum Electron.* **1978**, *21*, 728–739. [[CrossRef](#)]
29. Levush, B.; Antonsen, T.M.; Bromborsky, A.; Lou, W.R.; Carmel, Y. Theory of relativistic BWOs with end reflections. *IEEE Trans. Plasma Sci.* **1992**, *20*, 263–280. [[CrossRef](#)]
30. Miller, S.M.; Antonsen, T.M., Jr.; Levush, B.; Bromborsky, A.; Abe, D.K.; Carmel, Y. Theory of relativistic backward wave oscillators operating near cutoff. *Phys. Plasmas* **1994**, *1*, 730–740. [[CrossRef](#)]
31. Vlasov, A.N.; Nusinovich, G.S.; Levush, B. Effect of the zero spatial harmonic in a slow electromagnetic wave on operation of relativistic backward-wave oscillators. *Phys. Plasmas* **1997**, *4*, 1402–1412. [[CrossRef](#)]
32. Pierce, J.R. *Traveling Wave Tubes*, 1st ed.; Van Nostrand: Princeton, NJ, USA, 1950.
33. Rowe, J.E. *Nonlinear Electron-Wave Interaction Phenomena*; Academic Press: New York, NY, USA, 1965.
34. Ginzburg, N.S.; Zavol'skii, N.A.; Zapevalov, V.E.; Moiseev, M.A.; Novozhilova, Y.V. Nonstationary Processes in a Diffraction-Output Orottron. *Tech. Phys.* **2000**, *45*, 480. [[CrossRef](#)]
35. Nusinovich, G.S. *Introduction to the Physics of Gyrotrons*; J. Hopkins University Press: Baltimore, MD, USA, 2004.
36. Ginzburg, N.S.; Malkin, A.M.; Sergeev, A.S.; Zaslavsky, V.Y. Quasi-optical theory of relativistic submillimeter surface-wave oscillators. *Appl. Phys. Lett.* **2011**, *99*, 121505. [[CrossRef](#)]
37. Ginzburg, N.S.; Malkin, A.M.; Zheleznov, I.V.; Zaslavsky, V.Y.; Sergeev, A.S. Stimulated Cherenkov radiation of a relativistic electron beam moving over a periodically corrugated surface (quasi-optical theory). *J. Exp. Theor. Phys.* **2013**, *117*, 975–987. [[CrossRef](#)]
38. Ginzburg, N.S.; Malkin, A.M.; Zheleznov, I.V.; Sergeev, A.S. Evanescent waves propagation along a periodically corrugated surface and their amplification by relativistic electron beam (quasi-optical theory). *Phys. Plasmas* **2013**, *20*, 063105. [[CrossRef](#)]
39. Ginzburg, N.S.; Malkin, A.M.; Sergeev, A.S.; Zaslavsky, V.Y. Quasi-optical theory of relativistic surface-wave oscillators with one-dimensional and two-dimensional periodic planar structures. *Phys. Plasmas* **2013**, *20*, 113104. [[CrossRef](#)]
40. Malkin, A.M.; Zheleznov, I.V.; Sergeev, A.S.; Ginzburg, N.S. Quasi-optical theory of relativistic Cherenkov surface-wave oscillators with oversized cylindrical waveguides. *Phys. Plasmas* **2021**, *28*, 063102. [[CrossRef](#)]
41. Malkin, A.M.; Zheleznov, I.V.; Sergeev, A.S.; Zaslavsky, V.Y.; Makhlov, P.B.; Ginzburg, N.S. Unified quasi-optical theory of short-wavelength radiation amplification by relativistic electron beams moving near the impedance surfaces. *Phys. Plasmas* **2020**, *27*, 113106. [[CrossRef](#)]
42. Katsenelenbaum, B.Z.; del Rio, L.M.; Pereyaslavets, M.; Ayza, M.S.; Thumm, M. Theory of Nonuniform Waveguides: The Cross-section Method. *IET Electromagn. Waves Ser.* **1998**, *44*, 249.
43. Fedotov, A.E.; Makhlov, P.B. Transverse dynamics of a surface wave excited by a wide electron beam. *Phys. Plasmas* **2012**, *19*, 033103. [[CrossRef](#)]
44. Wang, Z.; Gong, Y.; Wei, Y.; Duan, Z. High-power millimeter-wave BWO driven by sheet electron beam. *IEEE Trans. Electron Dev.* **2013**, *60*, 471. [[CrossRef](#)]
45. Shin, Y.-M.; Zhao, J.; Barnett, L.R.; Luhmann, N.C. Investigation of terahertz sheet beam traveling wave tube amplifier with nanocomposite cathode. *Phys. Plasmas* **2012**, *17*, 123105. [[CrossRef](#)]
46. Shin, Y.-M.; Baig, A.; Barnett, L.R.; Luhmann, N.C.; Pasour, J.; Larsen, P. Modeling investigation of an ultrawideband terahertz sheet beam TWT amplifier Circuit. *IEEE Trans. Electron Dev.* **2011**, *58*, 3213–3218. [[CrossRef](#)]

47. Malkin, A.M.; Zaslavsky, V.Y.; Zhelezov, I.V.; Goykhman, M.B.; Gromov, A.V.; Palitsin, A.V.; Sergeev, A.S.; Fedotov, A.É.; Makhlov, P.B.; Ginzburg, N.S. Development of high-power millimeter-wave surface-wave generators based on relativistic ribbon electron beams. *Radiophys. Quantum Electron.* **2020**, *63*, 458. [[CrossRef](#)]
48. Leontovich, M.A. On the Approximate Boundary Conditions for the Electromagnetic Field on the Surface of Well Conducting Bodies. In *Investigations on Propagation of Radio Waves*; AN SSSR: Moscow, Russia, 1948; pp. 5–10.
49. Peskov, N.Y.; Ginzburg, N.S.; Golubev, I.I.; Golubykh, S.M.; Kaminsky, A.K.; Kozlov, A.P.; Malkin, A.M.; Sedykh, S.N.; Sergeev, A.S.; Sidorov, A.I.; et al. Powerful oversized W-band free-electron maser with advanced Bragg resonator based on coupling of propagating and cutoff waves. *Appl. Phys. Lett.* **2020**, *116*, 213505. [[CrossRef](#)]
50. Abramowitz, M.; Stegun, I. *Handbook of Mathematical Functions with Formulas, Graphs, and Mathematical Tables*, 6th ed.; U.S. Dept. of Commerce, National Bureau of Standards: Washington, DC, USA, 1972.
51. Ginzburg, N.S.; Malkin, A.M.; Sergeev, A.S.; Fil'chenkov, S.E.; Zaslavsky, V.Y. Highly selective surface-wave resonators for terahertz frequency range formed by metallic Bragg gratings. *Phys. Lett. A* **2018**, *382*, 925–929. [[CrossRef](#)]
52. Ginzburg, N.S.; Malkin, A.M.; Sergeev, A.S.; Zaslavsky, V.Y. Powerful surface-wave oscillators with two-dimensional periodic structures. *Appl. Phys. Lett.* **2012**, *100*, 143510. [[CrossRef](#)]
53. Ginzburg, N.S.; Malkin, A.M.; Sergeev, A.S.; Zaslavsky, V.Y. Oversized co-axial and cylindrical surface-wave oscillators with two-dimensional periodical grating (quasi-optical model). *J. Appl. Phys.* **2013**, *113*, 104504. [[CrossRef](#)]
54. Glyavin, M.Y.; Luchinin, A.G.; Nusinovich, G.S.; Rodgers, J.; Kashyn, D.G.; Romero-Talamas, C.A.; Pu, R. A 670 GHz gyrotron with record power and efficiency. *Appl. Phys. Lett.* **2012**, *101*, 153503. [[CrossRef](#)]
55. Ginzburg, N.S.; Novozhilova, Y.V.; Zotova, I.V.; Sergeev, A.S.; Peskov, N.Y.; Phelps, A.D.R.; Wiggins, S.M.; Cross, A.W.; Ronald, K.; He, W.; et al. Generation of powerful subnanosecond microwave pulses by intense electron bunches moving in a periodic backward wave structure in the superradiative regime. *Phys. Rev. E* **1999**, *60*, 3297. [[CrossRef](#)]
56. Eltchaninov, A.A.; Korovin, S.D.; Rostov, V.V.; Pegel, I.V.; Mesyats, G.A.; Rukin, S.N.; Shpak, V.G.; Yalandin, M.I.; Ginzburg, N.S. Production of short microwave pulses with a peak power exceeding the driving electron beam power. *Laser Part. Beams* **2003**, *21*, 187. [[CrossRef](#)]
57. Korovin, S.D.; Eltchaninov, A.A.; Rostov, V.V.; Shpak, V.G.; Yalandin, M.I.; Ginzburg, N.S.; Sergeev, A.S.; Zotova, I.V. Generation of Cherenkov superradiance pulses with a peak power exceeding the power of the driving short electron beam. *Phys. Rev. E* **2006**, *74*, 016501. [[CrossRef](#)] [[PubMed](#)]
58. Rostov, V.V.; Elchaninov, A.A.; Romanchenko, I.V.; Yalandin, M.I. A coherent two-channel source of Cherenkov superradiance pulses. *Appl. Phys. Lett.* **2012**, *100*, 224102. [[CrossRef](#)]
59. Shpak, V.G.; Shunailov, S.A.; Yalandin, M.I.; Dyad'kov, A.N. The RADAN SEF-303A, a small high-current pulsed power supply. *Instrum. Exp. Tech.* **1993**, *25*, 25031539.
60. Mesyats, G.A.; Yalandin, M.I. High-power picosecond electronics. *Physics-Uspekhi* **2007**, *48*, 211. [[CrossRef](#)]
61. Ginzburg, N.S.; Malkin, A.M.; Sergeev, A.S.; Zotova, I.V.; Zaslavsky, V.Y.; Zhelezov, I.V. 3D Quasioptical Theory of Terahertz Superradiance of an Extended Electron Bunch Moving Over a Corrugated Surface. *Phys. Rev. Lett.* **2013**, *110*, 184801. [[CrossRef](#)]
62. Ginzburg, N.S.; Malkin, A.M.; Sergeev, A.S.; Zhelezov, I.V.; Zotova, I.V.; Zaslavsky, V.Y.; Boltachev, G.S.; Sharypov, K.A.; Shunailov, S.A.; Ul'masculov, M.R.; et al. Generation of Subterahertz Superradiance Pulses Based on Excitation of a Surface Wave by Relativistic Electron Bunches Moving in Oversized Corrugated Waveguides. *Phys. Rev. Lett.* **2016**, *117*, 204801. [[CrossRef](#)]
63. Power, J.G. Overview of photoinjectors. In *AIP Conference Proceedings, Proceedings of 14th Advanced Accelerator Concepts Workshop, Annapolis, MD, USA, 13–19 June 2010*; Nusinovich, G., Gold, S., Eds.; American Institute of Physics: College Park, MD, USA, 2010; Volume 1299.
64. Piot, P.; Sun, Y.E.; Kim, K.J. Photoinjector generation of a flat electron beam with transverse emittance ratio of 100. *Phys. Rev. ST-AB* **2006**, *9*, 031001. [[CrossRef](#)]
65. Konoplev, I.V.; McGrane, P.; He, W.; Cross, A.W.; Phelps, A.D.R.; Whyte, C.G.; Ronald, K.; Robertson, C.W. Experimental Study of Coaxial Free-Electron Maser Based on Two-Dimensional Distributed Feedback. *Phys. Rev. Lett.* **2006**, *96*, 035002. [[CrossRef](#)]
66. Ginzburg, N.S.; Ilyakov, E.V.; Kulagin, I.S.; Malkin, A.M.; Peskov, N.Y.; Sergeev, A.S.; Zaslavsky, V.Y. Theoretical and experimental studies of relativistic oversized Ka-band surface-wave oscillator based on 2D periodical corrugated structure. *Phys. Rev. Accel. Beams* **2018**, *21*, 080701. [[CrossRef](#)]
67. Arzhannikov, A.V.; Ginzburg, N.S.; Kalinin, P.V.; Kuznetsov, S.A.; Malkin, A.M.; Peskov, N.Y.; Sergeev, A.S.; Sinitsky, S.L.; Stepanov, V.D.; Thumm, M.; et al. Using Two-Dimensional Distributed Feedback for Synchronization of Radiation from Two Parallel-Sheet Electron Beams in a Free-Electron Maser. *Phys. Rev. Lett.* **2016**, *117*, 114801. [[CrossRef](#)] [[PubMed](#)]
68. Ginzburg, N.S.; Zaslavsky, V.Y.; Malkin, A.M.; Sergeev, A.S.; Zotova, I.V.; Sharypov, K.A.; Shunailov, S.A.; Shpak, V.G.; Ul'masculov, M.R.; Yalandin, M.I. Generation of intense spatially coherent superradiant pulses in strongly oversized 2D periodical surface-wave structure. *Appl. Phys. Lett.* **2020**, *117*, 183505. [[CrossRef](#)]
69. Malkin, A.M.; Fedotov, A.E.; Zaslavsky, V.Y.; Fil'chenkov, S.E.; Sergeev, A.S.; Egorova, E.D.; Ginzburg, N.S. Relativistic sub-THz surface-wave oscillators with transverse Gaussian-like radiation output. *IEEE Electron Device Lett.* **2021**, *42*, 751. [[CrossRef](#)]
70. Ginzburg, N.S.; Malkin, A.M.; Zaslavsky, V.Y.; Fedotov, A.E.; Sergeev, A.S. Relativistic sub-THz surface-wave sheet-beam amplifier with transverse energy input and output. *IEEE Trans. Electron Devices* **2021**, *69*, 759. [[CrossRef](#)]